nature chemical biology

Article

https://doi.org/10.1038/s41589-025-01922-3

Programmable RNA acetylation with CRISPR–Cas13

Received: 29 December 2023

Accepted: 30 April 2025

Published online: 02 June 2025

Check for updates

Jihwan Yu[1], Juae Jin[1,5], Eury Kwon[1,5], Hyunsoo Jang[1,5], Sang-kun Choi[1], Donggyun Kim[1], Chaemin Kim[1], Seungkyu Son[1], Ki-Jun Yoon[1,2] & Won Do Heo[1,3,4]

Recent studies claim that N^4-acetylcytidine (ac^4C) modification of RNA confers crucial regulatory roles, such as increasing translation efficiency and prolonging its half-life. However, the absence of methods for selectively acetylating specific RNA molecules hampers linking ac^4C to cell physiology. Here, we developed an efficient molecular tool that incorporates ac^4C on a specific transcript of interest. Through protein engineering, we developed a hyperactive variant of *N*-acetyltransferase 10 (NAT10), designated enhanced NAT10 (eNAT10). When fused to the programmable RNA-targeting protein dCas13, eNAT10 enables robust acetylation of various target RNAs in multiple contexts. RNA acetylation by dCas13–eNAT10 was highly dependent on co-transfected guide RNA, highlighting its specificity. We also describe the programmable RNA chemical modification in vivo using dual-adeno-associated virus. Using our system, we found that acetylation of RNA may modulate the subcellular localization of modified transcripts. We anticipate that our tool will facilitate numerous studies on ac^4C functions across different cellular and disease contexts.

Over the last 60 years, more than 170 modifications on RNA have been discovered, and their regulatory roles have been extensively studied[1]. These modifications confer critical functions, including enhancing mRNA translation efficiency, prolonging transcript half-life and altering subcellular localization[2]. RNA modifications occur on all RNA species, and their altered patterns strongly correlate with various diseases[3].

N^4-Acetylcytidine (ac^4C), a prevalent RNA modification, occurs at conserved cytosines on 18S rRNA[4] and specific tRNAs[5]. Uniquely, ac^4C is the sole acetylation event on eukaryotic RNA and is catalyzed by *N*-acetyltransferase 10 (NAT10) and its homologs[6]. NAT10 is the only known human enzyme that harbors both acetyltransferase and nucleotide-binding domains[7].

In a recent study, Arango et al. detected and mapped ac^4C on human mRNA[8], demonstrating its critical roles in boosting translation efficiency and mRNA stabilization. Genetic ablation of *NAT10* resulted in significant downregulation of ac^4C-modified mRNAs, negatively impacting translation outcomes. Subsequent studies linked altered ac^4C modification patterns to viral infections[9–11], multiple types of cancer[12–15], neurological diseases[16,17] and many other cellular processes[18,19]. Although several lines of evidence have suggested that ac^4C on specific mRNA significantly contributes to the progression of multiple diseases, researchers have been unable to unequivocally demonstrate the regulatory importance of ac^4C itself because methods capable of writing ac^4C onto a specific transcript of interest have been lacking. Previous studies primarily relied on *NAT10*-knockout cell lines and chemical inhibition of NAT10 (ref. 20), both of which globally disrupt cellular RNA acetylation.

CRISPR–Cas systems constitute bacterial adaptive immune systems that selectively target and cleave exogenous nucleic acids[21]. In addition to the DNA-targeting Cas9 (ref. 22), the RNA-targeting CRISPR–Cas13 system[23] has generated substantial interest in the genome engineering field. Mutating two catalytic residues in Cas13 produces catalytically inactive dCas13 (ref. 24), which retains efficient RNA binding ability and programmability. dCas13 has been extensively

[1]Department of Biological Sciences, Korea Advanced Institute of Science and Technology (KAIST), Daejeon, Republic of Korea. [2]KAIST-Wonjin Cell Therapy Center, KAIST, Daejeon, Republic of Korea. [3]Department of Brain & Cognitive Sciences, KAIST, Daejeon, Republic of Korea. [4]KAIST Institute for the BioCentury (KIB), KAIST, Daejeon, Republic of Korea. [5]These authors contributed equally: Juae Jin, Eury Kwon, Hyunsoo Jang. e-mail: wondo@kaist.ac.kr

used for RNA imaging[25], RNA editing[26–28], writing and erasing RNA modifications[29–32] and many other applications[33–36].

We speculated that dCas13-guided NAT10 could specifically install ac^{4}C onto a target transcript in a programmable manner. The short guide RNA (gRNA) used with dCas13 allows efficient and flexible targeting of RNA, enabling researchers to study the functional impacts of acetylation on various endogenous transcripts. Due to the high specificity of the CRISPR–Cas13 system[23,24,26], dCas13-guided NAT10 would be expected to write ac^{4}C on desired transcripts but not on nontarget transcripts.

Here, we developed a method using fusion of rationally engineered human NAT10 to dCas13b, capable of acetylating target RNA in living cells and in vivo. Through a domain truncation study, we generated a highly active truncated NAT10 variant named enhanced NAT10 (eNAT10). dCas13–eNAT10 fusion protein could efficiently acetylate gRNA-targeted exogenous and endogenous cellular transcripts. Moreover, targeted acetylation by dCas13–eNAT10 enhanced protein production from modified mRNA. Specificity analysis using acetylated RNA immunoprecipitation and sequencing (acRIP–seq)[8,37] showed that off-target RNA acetylation was present but limited. Using a modified ac^{4}C-seq method[38,39], we mapped ac^{4}C residues at single-base resolution and verified the known sequence preferences of RNA acetylation. Furthermore, we developed inducible RNA acetylation systems and a dual-adeno-associated virus (AAV)-encoded intein-split RNA acetylation system for in vivo applications. Finally, we showed that ac^{4}C-modified transcripts are preferentially enriched in the cytoplasm, revealing a regulatory role for RNA acetylation in modulating subcellular RNA localization. This new tool is anticipated to significantly facilitate ac^{4}C research, overcoming limitations of prior approaches with its robustness and specificity.

Results

Design and evaluation of human NAT10 truncation variants

Human endogenous NAT10 is a relatively large (1,025 amino acids) protein that strongly localizes to the nucleolus[40]. To modulate the subcellular localization of NAT10 and identify a minimal unit that still retains RNA acetyltransferase activity, we cloned various NAT10 truncation variants fused to MS2-coat protein (MCP). Because the C terminus of NAT10 possesses a nucleolar localization signal[41] and disordered structure[42], we generated C-terminal truncation variants. We tethered MCP–NAT10 fusion proteins to reporter transcripts with two MS2 stem loops and measured the degree of RNA acetylation using acetylated RNA immunoprecipitation followed by quantitative PCR (acRIP–qPCR[8]; Fig. 1a).

Full-length NAT10 fused to MCP showed 40-fold enrichment of target RNA in samples immunoprecipitated with anti-ac^{4}C compared to samples immunoprecipitated with isotype control (Fig. 1b). The shortest C-terminal truncation tested, Δ921–1025, modestly improved RNA acetylation (51-fold enrichment), likely by removing the native nucleolar localization signal and enhancing cytoplasmic mRNA access. Surprisingly, additional deletion of the disordered C-terminal region and most of the tRNA-binding domain substantially improved RNA acetyltransferase activity. The Δ802–1025 variant exhibited 127-fold enrichment of target RNA, achieving the strongest RNA acetylation signal among all truncation variants tested. Further C-terminal deletion was detrimental to activity. RNA acetyltransferase activity of NAT10 truncation variants was not correlated with their expression levels (Supplementary Fig. 1a,b). Based on these observations, we chose the hyperactive Δ802–1025 variant, designated eNAT10, for use in subsequent development of a programmable RNA acetylation system.

Interestingly, minimal N-terminal truncation (Δ1–72), mimicking the NAT10 isoform b (NP_001137502) present in human cells, completely abolished RNA acetylation (Fig. 1b). Although previous studies reported protein acetyltransferase activity retention in similar isoforms[40,43], our results indicate a critical role for NAT10's N-terminal region in RNA acetyltransferase function, supporting previous assertions that RNA is the preferred substrate of N-terminus-retaining NAT10 isoforms[8].

Because helicase (ATPase) function and K426 autoacetylation are essential for NAT10's RNA acetyltransferase activity[9], we tested corresponding mutation in eNAT10. Indeed, K290A (helicase-inactive), K426R (autoacetylation-deficient) and G641E (acetyltransferase-inactive, designated edNAT10) mutations abolished activity (Extended Data Fig. 1a), suggesting that helicase (ATPase) activity and autoacetylation of eNAT10 are essential for RNA acetylation. Despite truncation, eNAT10 maintains NAT10's core structure (Extended Data Fig. 1b), further validating functional similarity.

Because of its inherent localization signals, MCP-fused full-length NAT10 mostly localized to the nucleolus, regardless of an additional nuclear export signal (NES) or nuclear localization signal (NLS) fusion (Fig. 1c). Subcellular localization of various NAT10–enhanced green fluorescent protein (NAT10–eGFP) fusions confirmed this (Supplementary Fig. 2a,b). Notably, NES-fused eNAT10 exclusively localized to the cytoplasm, and the corresponding NLS fusion predominantly localized to the nucleoplasm (Fig. 1d). Thus, fusion of localization signals to eNAT10 robustly directs its subcellular distribution, enabling targeted acetylation of specifically localized RNAs.

To evaluate protein translation impacts of targeted RNA acetylation, we measured protein production from MCP–NES–eNAT10-targeted mRNA compared to the catalytically inactive MCP–NES–edNAT10-G641E-targeted control. We used mCherry-encoding reporter transcript with two MS2 stem loops at the 3′ untranslated region (3′ UTR; Fig. 1e). Flow cytometry analysis showed elevated translation of the ac^{4}C-modified mCherry transcript relative to that of the nontarget EBFP2 (Fig. 1f and Extended Data Fig. 1d). Compared to control samples, a 1.4-fold increase in translation of the reporter by MCP–NES–eNAT10 targeting was observed. Luciferase assays targeting firefly luciferase (Fluc) transcripts fused to MS2 hairpins corroborated these findings (Extended Data Fig. 1c).

Together, these results demonstrate successful engineering of a hyperactive RNA acetyltransferase (eNAT10) capable of robust targeted RNA acetylation. We further validated effective control over eNAT10 subcellular localization and confirmed that RNA acetylation significantly enhances translation efficiency, highlighting the major regulatory mechanism of mRNA acetylation.

Characterization of the dCas13–eNAT10 fusion protein

To confer programmability to the target RNA acetylation system, we fused hyperactive eNAT10 to dCas13, which selectively binds to target transcripts via gRNA (Fig. 2a). We specifically used dPspCas13b for its robust targeting efficiency and specificity[26,29]. We constructed NES- and NLS-fused dCas13–eNAT10, with a flexible XTEN linker inserted between localization signals and eNAT10 (Extended Data Fig. 2a). An mCherry reporter with a short λ bacteriophage sequence (lambda2) at its 3′ UTR served as the initial target RNA[44,45].

In its NES and NLS configurations, dCas13–eNAT10 showed 109-fold and 52-fold enrichment of target RNA, respectively, from acRIP–qPCR in 293T cells co-transfected with lambda2 gRNA (Fig. 2b). By contrast, dCas13–NAT10 fusions showed only two- to threefold enrichment of target RNA. Controls with nontargeting gRNA or catalytically inactive edNAT10 produced basal levels of target RNA acetylation. The nontargeted reporter transcript *EBFP2* also showed marginal levels of RNA acetylation, confirming the specificity (Extended Data Fig. 2b). Luciferase assays confirmed increased protein translation following targeted acetylation of Fluc-lambda2 reporter (Extended Data Fig. 2c).

We further validated RNA acetylation efficiency across HeLa, NIH3T3 and N2a cell lines and rat primary astrocytes (Extended Data

https://doi.org/10.1038/s41589-025-01922-3

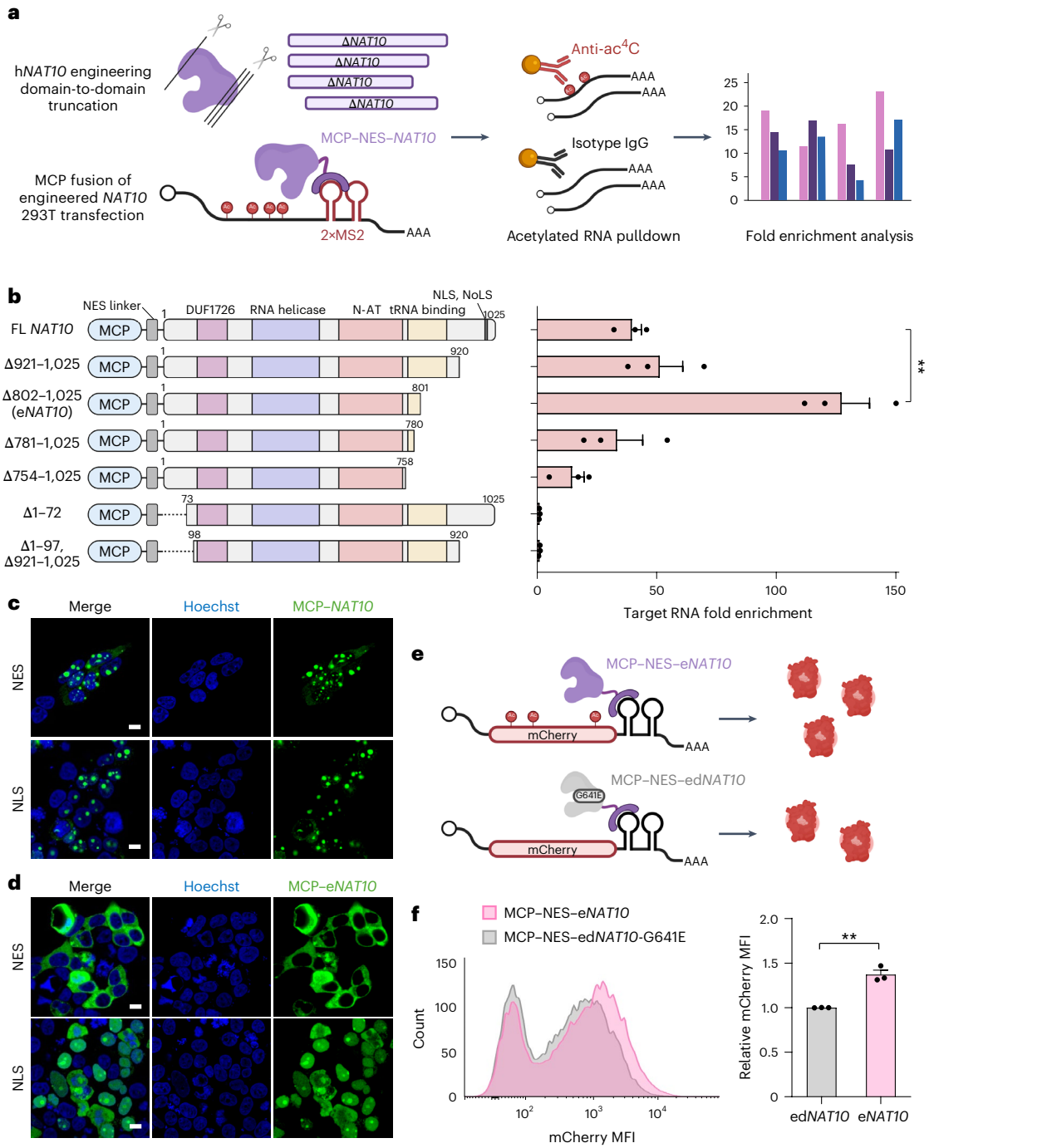

Fig. 1 | Engineering of human NAT10 yields the hyperactive RNA acetyltransferase eNAT10. a, Schematic of the NAT10 engineering and subsequent RNA acetylation activity comparison with acRIP; FL, full-length; hNAT10, human NAT10. **b**, Schematic of NAT10 truncation variants fused to MCP and their target RNA acetylation activity measured by acRIP–qPCR. 293T cells were transfected with MCP–NAT10 variants with Fluc–2×MS2 reporter. Data are presented as mean ± s.e.m. from three biologically independent replicates. Significance was calculated by two-tailed Student's *t*-test; $^{**}P < 0.01$ ($P = 2.00 \times 10^{-3}$). **c**,**d**, Subcellular localization of MCP–NAT10–Flag (**c**) and MCP–eNAT10–Flag (**d**) fusion proteins. Images were acquired after paraformaldehyde (PFA) fixation, permeabilization of transfected 293T cells and immunostaining of the Flag tag; scale bars, 10 μm. **e**, Schematic of ac^{4}C-mediated upregulation of mCherry–2×MS2 reporter translation. **f**, Flow cytometry results of MCP–NES–eNAT10 (or edNAT10) targeted mCherry reporter in 293T cells. A representative histogram (left) and EBFP2-normalized mCherry mean fluorescence intensity (MFI; right) are shown. Data are presented as mean ± s.e.m. from three biologically independent replicates. Significance was calculated by two-tailed Student's *t*-test; $^{**}P < 0.01$ ($P = 1.67 \times 10^{-3}$).

Fig. 2d–g). Although acetylation levels varied, robust target RNA acetylation occurred in cells co-transfected with dCas13–eNAT10 and lambda2 gRNA. NES fusion generally showed greater efficiency, likely due to the predominant cytoplasmic localization of reporter mRNA.

To determine whether our tool can acetylate endogenous RNAs, we designed several gRNAs targeting various human endogenous RNAs and transfected them together with dCas13–eNAT10. Both NES-fused protein-targeting cytoplasmic mRNAs and NLS-fused protein-targeting nuclear long noncoding RNAs (lncRNAs) showed gRNA-dependent target RNA acetylation (Fig. 2c). The highest RNA acetylation signals were observed for *FUS* and *PTEN* mRNA, which showed 16- and 12-fold enrichments by acRIP–qPCR, respectively. Nuclear lncRNAs showed

https://doi.org/10.1038/s41589-025-01922-3

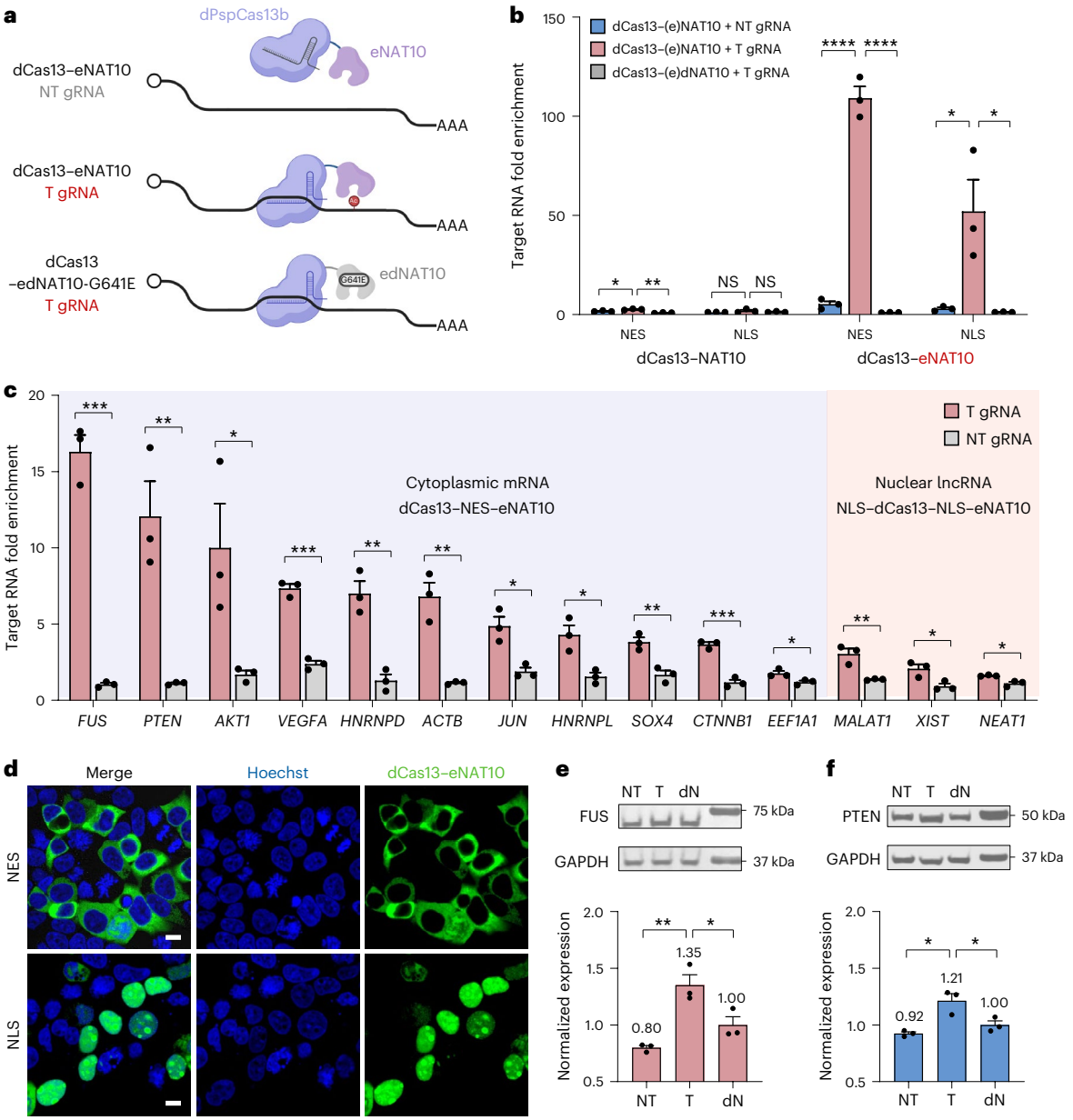

Fig. 2 | Development of the PspCas13b-directed target RNA acetylation system. a, Schematic illustration of dCas13–eNAT10 fusion proteins binding to target RNA. Target RNA is acetylated only in the presence of reporter-targeting gRNA (T gRNA) and catalytically active dCas13–eNAT10; NT, nontargeting. **b**, mCherry-lambda2 reporter RNA acetylation by dCas13–NAT10 and dCas13–eNAT10 fusion proteins in 293T cells, measured by acRIP–qPCR. Data are presented as mean ± s.e.m. from three biologically independent replicates. Significance was calculated by two-tailed Student's *t*-test; NS, not significant ($P = 2.18 \times 10^{-1}$ and 3.29×10^{-2}, from left to right); $^{*}P < 0.05$ ($P = 2.88 \times 10^{-2}$, 3.71×10^{-2} and 3.34×10^{-2}, from left to right); $^{**}P < 0.01$ ($P = 1.13 \times 10^{-3}$); $^{****}P < 0.0001$ ($P = 6.59 \times 10^{-5}$ and 4.99×10^{-5}, from left to right). **c**, Programmable acetylation of endogenous RNAs using NES- or NLS-fused dCas13–eNAT10 in 293T cells. RNA acetylation signals were measured by acRIP–qPCR. Data are presented as mean ± s.e.m. from three biologically independent replicates. Significance was calculated by two-tailed Student's *t*-test; $^{*}P < 0.05$ ($P = 4.63 \times 10^{-2}$, 1.11×10^{-2}, 1.58×10^{-2}, 3.13×10^{-2}, 2.81×10^{-2} and 1.02×10^{-2}, from left to right); $^{**}P < 0.01$ ($P = 8.73 \times 10^{-3}$, 3.17×10^{-3}, 3.51×10^{-3}, 6.91×10^{-3} and 8.81×10^{-3}, from left to right); $^{***}P < 0.001$ ($P = 1.58 \times 10^{-4}$, 1.66×10^{-4} and 4.73×10^{-4}, from left to right). **d**, Subcellular localization of dCas13–eNAT10–Flag fusion proteins containing NES or NLS imaged after PFA fixation and permeabilization of transfected 293T cells and immunostaining of Flag tag; scale bars, 10 µm. **e**,**f**, Expression levels of endogenous FUS (**e**) and PTEN (**f**) targeted with dCas13–NES–eNAT10 in 293T cells. For FUS targeting, dual guides (gFUS-1 and gFUS-2) were used simultaneously. Representative blots (top) and quantification of normalized expression levels of each protein (bottom) are shown. Data are presented as mean ± s.e.m. from three biologically independent replicates. Significance was calculated by two-tailed Student's *t*-test; $^{*}P < 0.05$ ($P = 4.12 \times 10^{-2}$, 1.05×10^{-2} and 4.06×10^{-2}, from left to right); $^{**}P < 0.01$ ($P = 4.34 \times 10^{-3}$); dN, edNAT10.

generally lower acetylation (two- to threefold), possibly due to their structural complexity and multiple RNA-binding proteins, which might disturb dCas13–target RNA binding interactions[46]. NLS fusion targeting of endogenous mRNA also showed gRNA-dependent RNA acetylation patterns (Extended Data Fig. 3e), but the acetylation efficiency was generally lower than the NES fusion.

We next investigated whether targeting a single transcript with dual guides could enhance acetylation efficiency. Transfection of dual guides each at half doses successfully increased the RNA acetylation of exogenous (Fluc-lambda2) and endogenous (*FUS*, *ACTB*) transcripts compared to single-guide targeting (Extended Data Fig. 3a–c), also enhancing the translational outcome of Fluc-lambda2 (Extended Data Fig. 3d).

Similar to MCP–NAT10 fusion proteins, dCas13–NAT10 fusions retained a significant degree of nucleolar localization (Supplementary Fig. 3). By contrast, dCas13–eNAT10 fusions localized to intended compartments (Fig. 2d). Precise control of dCas13–eNAT10 localization allows for targeting of various endogenous RNAs in specific subcellular locations.

To measure ac^{4}C-mediated translational upregulation of endogenous genes, we performed western blotting of FUS and PTEN. For targeting of *FUS* mRNA, we used dual guides (gFUS-1 and gFUS-2) for more efficient ac^{4}C installation. Modest but statistically significant increases in protein expression (1.2- to 1.3-fold) compared to catalytically inactive edNAT10 samples were observed in 293T cells transfected with dCas13–NES–eNAT10 and targeting gRNAs (Fig. 2e,f). Additional gRNA screening and optimization of multiple gRNAs may increase both RNA acetylation signal and translational upregulation of endogenous genes of interest.

Specificity of the dCas13–eNAT10 fusion protein

To evaluate the specificity, we characterized transcriptome-wide off-target acetylation of RNA in 293T cells using acRIP–seq[8,37] (Extended Data Fig. 4a, NES acRIP–seq). Initial validation by qPCR with reverse transcription (RT–qPCR) confirmed that sequenced samples showed patterns of target RNA acetylation similar to that of our previous experiment (Extended Data Fig. 4b). Genes with 'differential RNA acetylation' were defined by an average transcripts per million (TPM) count of >10, adjusted *P* value of <0.05 and ac^{4}C fold change of >2 between sample groups. Active eNAT10 expression yielded 800 to 851 differential RNA acetylations compared to catalytically inactive edNAT10 (Fig. 3b,c).

Comparatively fewer differential RNA acetylations were observed between samples and only differed with transfected gRNA (Fig. 3a), suggesting that most off-target acetylation must have occurred in a gRNA-independent manner, probably owing to the intrinsic substrate preference of eNAT10. For instance, *POLR2A* transcripts consistently exhibited elevated acetylation regardless of gRNA (Extended Data Fig. 4c), whereas endogenous transcripts targeted in Fig. 2c showed no off-target acetylation (Extended Data Fig. 4d). Interestingly, *RPS16* mRNA, which has not been reported to undergo acetylation in human cells[8], was modestly acetylated following dCas13–eNAT10 expression. Collectively, our acRIP–seq results demonstrate that dCas13–NES–eNAT10 showed limited transcriptome-wide off-target acetylation.

We also performed acRIP–seq with total RNA from NLS–dCas13–NLS–eNAT10-transfected 293T cells (NLS acRIP–seq). The NLS fusion yielded fewer off-target events (276 differential acetylations) than NES fusions (Extended Data Fig. 5a). To directly compare the specificity of NES and NLS fusions, we measured the RNA acetylation levels of 13 highly acetylated genes (defined from acRIP–seq results) using acRIP–qPCR. In both contexts of exogenous mCherry-lambda2 reporter targeting and endogenous *FUS* targeting, NES fusion showed higher off-target RNA acetylation (Extended Data Fig. 5b). These results suggest that, despite the efficiency drop, utilization of the nuclear version of our tool can restrict off-target acetylation. Importantly, off-target RNA acetylation levels did not vary between exogenous and endogenous RNA-targeting contexts, further suggesting that most off-target RNA acetylation is occurring in a gRNA-independent manner.

To assess potential cellular perturbations, we also performed total RNA sequencing on 293T cells transfected with dCas13–NES–eNAT10 (Supplementary Fig. 4a). The two sample groups showed highly similar transcriptomic profiles (Pearson coefficient = 0.997) and limited differentially expressed genes (Fig. 3d and Supplementary Fig. 4a–c). Furthermore, immunostaining of pan-acetyl-lysine showed no significant changes in global protein acetylation levels following eNAT10 overexpression compared to controls (Fig. 3e).

To orthogonally evaluate ac^{4}C levels, we performed liquid chromatography–tandem mass spectrometry (LC–MS/MS) of various RNA fractions isolated from tool-expressing cells. Importantly, RNA from wild-type HeLa cells showed significantly higher ac^{4}C/C ratios than RNA from *NAT10*-knockout HeLa cells, validating our experimental scheme (Supplementary Fig. 5a). To specifically analyze target RNA acetylation with LC–MS/MS, we constructed a reporter fused with four streptavidin-binding aptamers[47] (mCherry-lambda2–4×S1m). Total RNA was isolated from reporter- and tool-expressing cells, and the reporter mRNA was enriched by streptavidin pulldown. LC–MS/MS analysis of enriched target RNA showed insignificant but increased ac^{4}C/C ratios from lambda2 gRNA-transfected samples compared to nontargeting gRNA-transfected samples (Supplementary Fig. 5b).

We next measured the ac^{4}C levels of total RNA (Fig. 3f), poly(A) RNA (Fig. 3g) and the small RNA fraction (Supplementary Fig. 5c) of tool-transfected 293T cells. As expected, the average ac^{4}C/C ratio was highest in small RNA, likely due to the acetylated tRNAs, and lowest in poly(A) RNA. However, overexpression of the catalytically active version of our tool did not perturb global ac^{4}C levels across all RNA species.

Given that RNA acetylation is known to increase translation efficiency of modified mRNA[8], we performed quantitative whole-proteome analysis of dCas13–NES–eNAT10-transfected 293T cells. Among 5,105 identified proteins, 84 were upregulated in dCas13–NES–edNAT10-expressing cells, and 116 were upregulated in dCas13–NES–eNAT10-expressing cells (Fig. 3h). Among the 13 previously specified highly acetylated genes (Extended Data Fig. 5b), 12 were detected by LC–MS/MS. On average, these genes exhibited a 1.12-fold higher protein expression in cells transfected with dCas13–NES–eNAT10 (Supplementary Fig. 5d). Although the increase in protein expression is limited, we recommend that researchers carefully reanalyze LC–MS/MS results to determine whether their gene of interest might be influenced by overexpression of the tool.

Comprehensively, our rigorous evaluations including transcriptome-wide acRIP–seq, RNA sequencing (RNA-seq), pan-acetyl-lysine staining, nucleoside LC–MS/MS and whole-proteome profiling indicate that the hyperacetylation activity of eNAT10 is unlikely to significantly perturb transfected cells, at least when fused to the specific RNA-binding protein dCas13b. However, inclusion of nontargeting controls in experiments remains highly recommended to precisely assess specific effects of targeted RNA acetylation.

Single-base mapping of dCas13–eNAT10-written ac^{4}C

To analyze the specific acetylation residues of target RNA at a single-base resolution, we modified an existing ac^{4}C-seq protocol[38,39] that uses $NaCNBH_3$ to reduce acetylated cytidines in RNA. $NaCNBH_3$-reduced ac^{4}C is efficiently converted into N^4-tetrahydroacetylcytidine, which is misread by reverse transcriptase and ultimately leads to a C-to-T conversion of acetylated residues that can be detected by cDNA sequencing.

Before applying $NaCNBH_3$, we enriched acetylated RNAs from total RNA samples using acRIP (Fig. 4a). Additionally, we optimized reverse transcription temperature to maximize C-to-T misincorporation efficiency, referring to a similar protocol[48,49] (Extended Data Fig. 6a–g). Whereas no apparent C-to-T conversions were observed in untreated control samples (Extended Data Fig. 6b and Supplementary Fig. 6c–h), targeted Illumina sequencing confirmed $NaCNBH_3$-dependent C-to-T conversions at acetylated cytidines in mCherry-lambda2 transcripts targeted by dCas13–NES–eNAT10 (Fig. 4b and Supplementary Fig. 7a). Although the resulting conversion rates may overestimate the levels of cytidine acetylation in living cells, acRIP enrichment enabled us to clearly distinguish the acetylated residue from sequencing noise (Supplementary Fig. 6a). Among the 14 ac^{4}C-modified residues with >1% C-to-T conversion rates, the most efficiently modified residue showed 20.6% C-to-T conversion. Motif analysis of modified residues showed a preference for 5′-CCG-3′ (Fig. 4c). Remarkably, all of the top three modified residues of the mCherry-lambda2 reporter possessed this motif.

For Fluc-lambda2 transcripts targeted by dCas13–NES–eNAT10, 23 residues exhibited ≥1% conversion, with the 6 highest (>5%) containing

https://doi.org/10.1038/s41589-025-01922-3

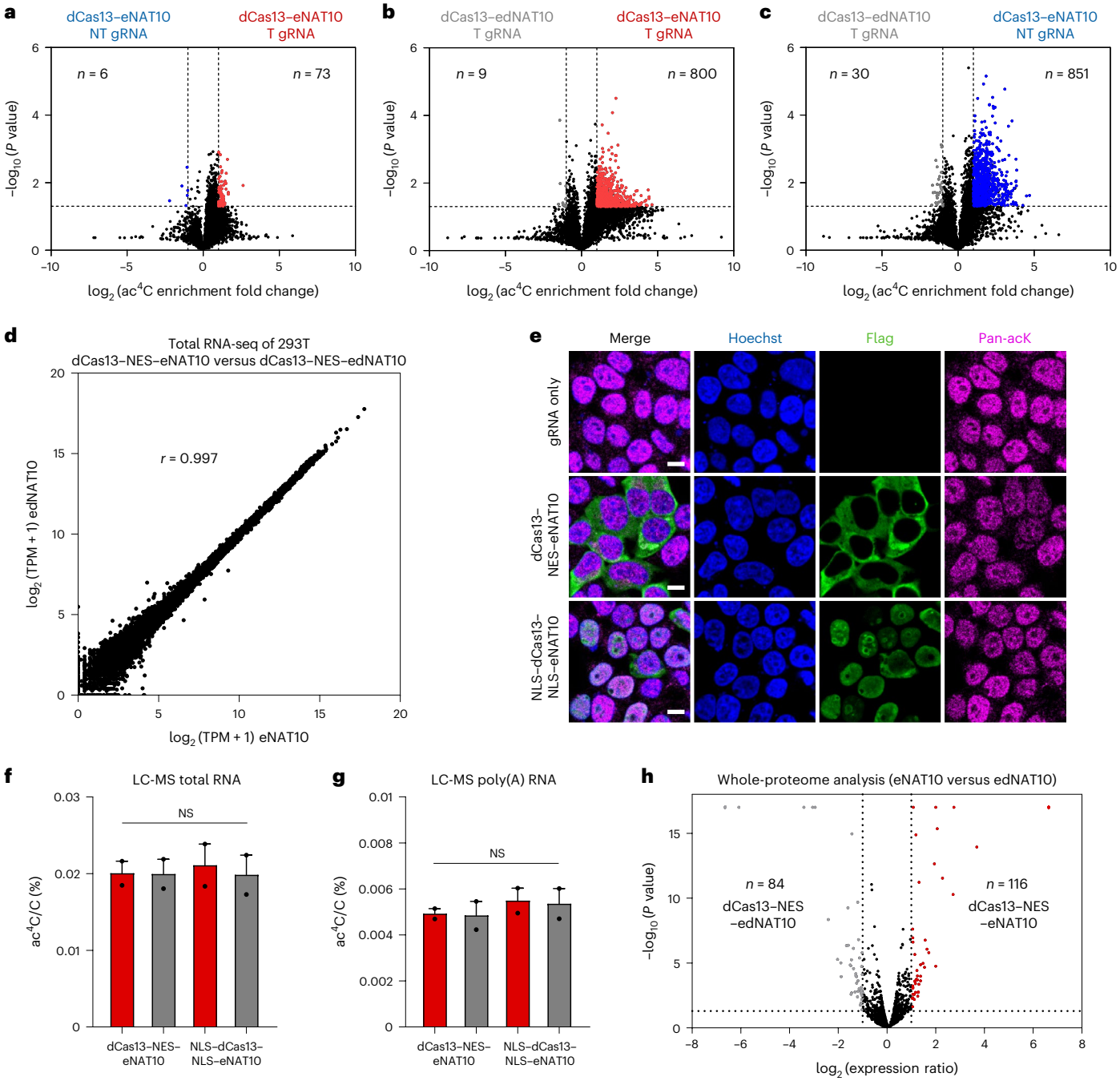

Fig. 3 | Specificity of the target RNA acetylation system in human cells. **a**–**c**, Transcriptome-wide analysis of off-target acetylation in 293T cells transfected with dCas13–NES–eNAT10 (or edNAT10) with nontargeting gRNA (NT gRNA) or lambda2-targeting gRNA (T gRNA). Numbers of genes with differential ac^4C enrichment are annotated in each graph (acRIP–seq average TPM cutoff: 10, *P* value cutoff: 0.05, ac^4C enrichment fold change cutoff: twofold). acRIP–seq was performed using three independent biological replicates for each sample group. **d**, Expression levels of all transcripts in 293T cells transfected with dCas13–NES–eNAT10 or dCas13–NES–edNAT10; Pearson coefficient $r = 0.997$. RNA sequencing was performed using three independent biological replicates for each sample group. **e**, Pan-acetyl-lysine levels of cells transfected with dCas13–eNAT10. Cells were imaged after PFA fixation, permeabilization and immunostaining of Flag tag (green) and pan-acetyl-lysine (pan-acK; pink); scale bars, 10 µm. **f**,**g**, Quantification of ac^4C/C ratios in 293T cells transfected with the NES or NLS version of the tool by LC–MS/MS. Quantification from total RNA (**f**) and enriched poly(A) RNA (**g**) was performed. Red bars indicate eNAT10 fusion, and gray bars indicate edNAT10 fusion. Data are presented as mean ± s.e.m. from two biologically independent replicates. Significance was calculated by two-tailed Student's *t*-test (NS, $P > 0.05$). **h**, Quantitative whole-proteome analysis of 293T cells transfected with dCas13–NES–eNAT10 or dCas13–NES–edNAT10 using LC–MS/MS. Numbers of genes with differential protein expression are annotated (*P* value cutoff: 0.05, expression fold change cutoff: twofold). Analysis was performed using two independent biological replicates for each sample group.

the 5′-CCG-3′ motif (Supplementary Figs. 6b and 7b,c). These results indicate that, although 5′-CCG-3′ is not an absolutely required motif for RNA acetylation[50,51], it is a highly preferred motif, as described by previous reports[38,52].

To see whether the sequence motif is a major determinant of RNA acetylation, we mutated the original mCherry-lambda2 reporter with three highly modified 5′-CCG-3′ residues (147C, 474C and 742C) to construct two distinctly mutated mCherry-lambda2 reporters: 3×CAG and

https://doi.org/10.1038/s41589-025-01922-3

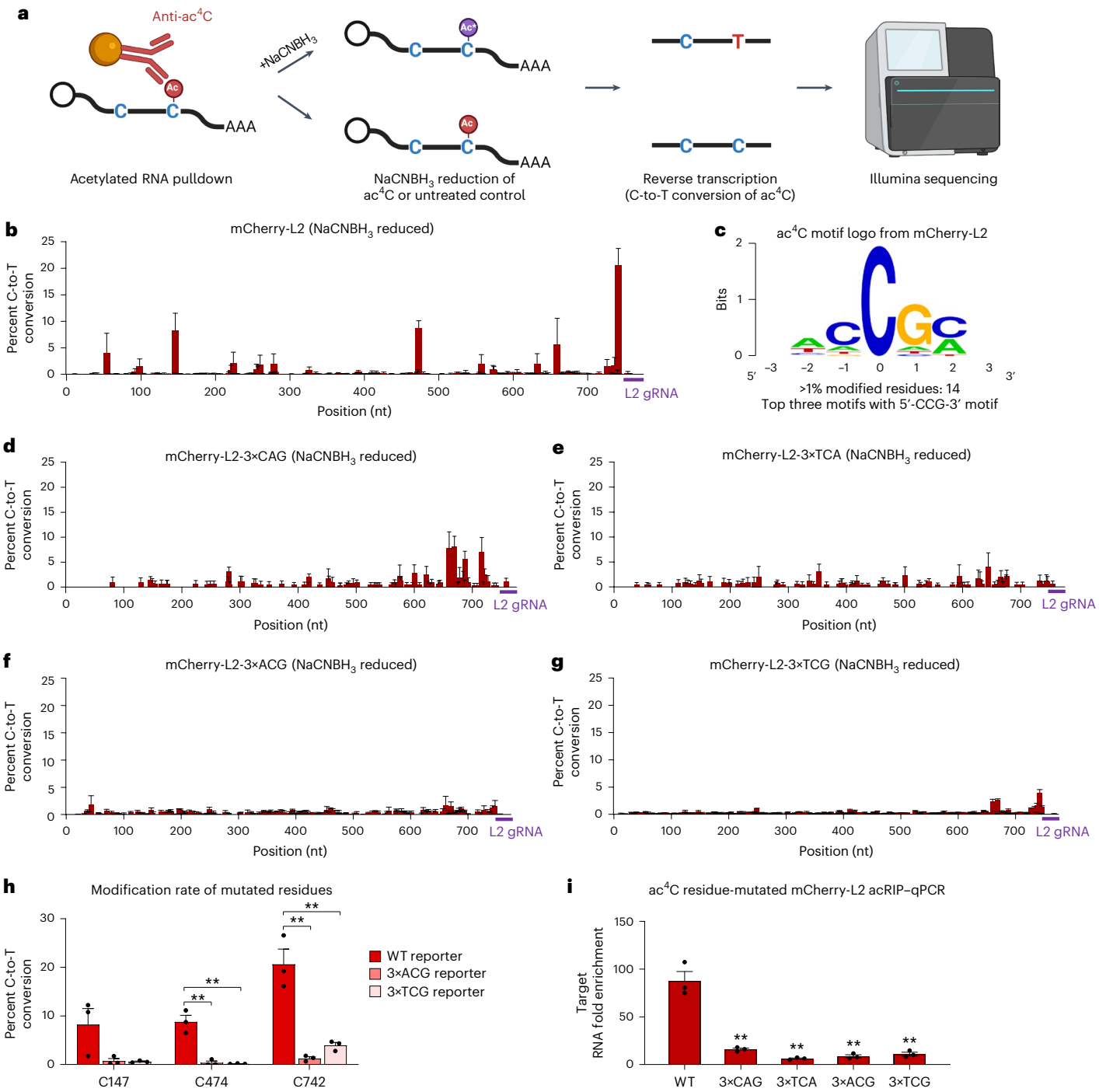

Fig. 4 | Single-base mapping of eNAT10-written ac^{4}C. a, Schematic illustration of single-base-resolution ac^{4}C mapping using $NaCNBH_3$ RT–PCR sequencing. RNA from 293T cells transfected with dCas13–NES–eNAT10 and gRNAs was processed with acRIP, followed by $NaCNBH_3$ treatment, reverse transcription, PCR amplification of targeted transcripts and Illumina sequencing. **b**, C-to-T conversion levels of mCherry-lambda2 (L2) reporter mRNA targeted with dCas13–NES–eNAT10. Data are presented as mean ± s.e.m. from three biologically independent replicates; nt, nucleotides. **c**, Sequence logo of C-to-T-converted sites from **b**. Twenty-one-nucleotide sequences flanking C-to-T-converted bases were analyzed. A 7-nucleotide-long sequence logo was created. **d**–**g**, C-to-T conversion levels of the top three ac^{4}C-modified motif-mutated mCherry-lambda2 reporter variants targeted with dCas13–NES–eNAT10. The 3×CAG reporter (**d**), 3×TCA reporter (**e**), 3×ACG reporter (**f**) and 3×TCG reporter (**g**) are shown. Data are presented as mean ± s.e.m. from three biologically independent replicates. Positions of gRNAs are annotated in purple. **h**, C-to-T conversion rates of central cytidines of mutated motifs from wild-type, 3×ACG and 3×TCG reporters. Data are presented as mean ± s.e.m. from three biologically independent replicates. Significance was calculated by two-tailed Student's *t*-test; $^{**}P < 0.01$ ($P = 3.72 \times 10^{-3}$, 3.00×10^{-3}, 3.40×10^{-3} and 6.10×10^{-3}, from left to right). **i**, acRIP–qPCR results of wild-type and mutated mCherry-lambda2 reporters targeted with dCas13–NES–eNAT10 and lambda2-targeting gRNA. Data are presented as mean ± s.e.m. from three biologically independent replicates. Statistical significance compared to the wild-type reporter group was calculated by two-tailed Student's *t*-test; $^{**}P < 0.01$ ($P = 2.04 \times 10^{-3}$, 1.24×10^{-3}, 1.44×10^{-3} and 1.65×10^{-3}, from left to right).

3×TCA. Whereas 3×CAG reporter lacks the central cytidine at preferred acetylation residues, the 3×TCA reporter harbors a less-preferred acetylation motif from the mCherry-lambda2 motif analysis.

The new reporters showed different patterns of RNA acetylation following dCas13–NES–eNAT10 targeting (Fig. 4d,e). The 3×CAG reporter showed new acetylated residues (660C, 669C, 687C and 716C) with >5% C-to-T conversions, two of which possessed the 5′-CCG-3′ motif. The 5′ cytidines of mutated motifs (5′-CAG-3′) showed no acetylation signal. Interestingly, acetylation at the three previously top-modified cytidines (5′-TCA-3′) was completely abolished in the 3×TCA reporter. These results were further validated by Sanger sequencing of PCR-amplified cDNA fragments (Supplementary Fig. 8). If the conformational advantage of certain residues following dCas13–eNAT10 targeting was a major determinant of RNA acetylation, 5′ adjacent cytidines of 3×CAG motifs and central cytidines of 3×TCA motifs should also be acetylated at least to some degree, regardless of the surrounding sequence motif. However, our results indicate that the 5′-CCG-3′ sequence motif itself is highly preferred for RNA acetylation.

Recent reports suggest that the 5′-NCG-3′ motif, rather than the 5′-CCG-3′ motif, can be preferentially acetylated in various organisms[18,51]. We constructed additional mCherry-lambda2 reporters harboring three 5′-ACG-3′ motifs (3×ACG reporter) or three 5′-TCG-3′ motifs (3×TCG reporter), replacing the three highly modified 5′-CCG-3′ residues from the original reporter. Overall C-to-T conversion rates of these mutated reporters were decreased compared to the original reporter (Fig. 4f,g). Although 5′-ACG-3′ and 5′-TCG-3′ could indeed be modified, two of three central cytidines of mutated residues (C474, C742) showed significantly decreased C-to-T conversion rates (Fig. 4h). Moreover, compared to the original reporter, acRIP–qPCR enrichment of all four mutated reporters was significantly decreased (Fig. 4i). Collectively, single-base mapping of eNAT10-written ac^{4}C revealed that 5′-CCG-3′ is a highly preferred acetylation motif, and mutation of ac^{4}C residues can disrupt RNA acetylation patterns of modified transcripts.

We extended single-base ac^{4}C mapping to various targets without acRIP enrichment due to the cDNA amplification challenges after treatment. Mapping of the Fluc–2×MS2 reporter targeted with MCP and truncated NAT10 fusion proteins showed a clear increase in C-to-T conversion exclusively in MCP–eNAT10 samples (Supplementary Fig. 9a–d). Endogenous mRNA targeting using dCas13–NES–eNAT10 and corresponding gRNA yielded generally higher average C-to-T conversion rates across amplified regions of target transcripts than nontargeting gRNA-transfected samples (Supplementary Fig. 9e–k). However, it is important to note that ac^{4}C mapping with $NaCNBH_3$ treatment, without acRIP enrichment of acetylated RNA, struggles to precisely distinguish acetylated residues from sequencing noise. On the other hand, incorporating an acRIP enrichment step makes it more challenging to amplify full-length transcripts with low cellular expression because $NaCNBH_3$ treatment induces rapid RNA degradation[51]. Adopting a recently reported RetraC:T-seq protocol[53] may boost the C-to-T conversion efficiency following $NaCNBH_3$ reduction of acetylated RNA.

To comprehensively profile off-target RNA acetylation residues when our tool is overexpressed, we conducted transcriptome-wide ac^{4}C-seq. Specific increases in C-to-T mismatch abundance after $NaCNBH_3$ treatment was observed from ac^{4}C-seq results of dCas13–NES–eNAT10-transfected 293T cells (Extended Data Fig. 7a). Additionally, we defined significantly mismatched residues based on three criteria: >10 aligned read counts, >3 mismatched read counts and mismatch rates exceeding 1.25%. Among all mismatch types, the number of significantly C-to-T mismatched residues was highest specifically in the $NaCNBH_3$-treated samples (Extended Data Fig. 7b).

From the ac^{4}C-seq results, selected highly acetylated genes (Extended Data Fig. 5b) showed increased C-to-T conversion rates with active eNAT10 expression (Extended Data Fig. 7c–l). Importantly, transcripts requiring gRNA for targeted acetylation, as well as *GAPDH* mRNA, which has not been reported to undergo acetylation in human cells[8], did not display elevated C-to-T conversions (Supplementary Fig. 10a–f). Our ac^{4}C-seq results further highlight that single-base ac^{4}C mapping should be performed with appropriate control samples (for example, $NaCNBH_3$-untreated samples and catalytically inactive edNAT10-transfected samples) to distinguish truly acetylated residues from single-nucleotide polymorphisms, endogenous C-to-U RNA editing and potential nucleobase deamination caused during RNA chemical treatment, as suggested by previous reports[51,54].

Inducible and reversible target RNA acetylation

Control of target RNA acetylation using inducers would enable spatiotemporal regulation of RNA acetylation with high precision and specificity. Therefore, we constructed small-molecule-inducible RNA acetylation systems by fusing ABI and PYL1 (refs. 55,56) to dPspCas13b and eNAT10, respectively. ABI and PYL1 are binding partners that efficiently dimerize in the presence of the plant hormone abscisic acid (ABA), which has no reported mammalian endogenous targets. Indeed, addition of 100 μM ABA to 293T cells co-transfected with dCas13–ABI and PYL1–eNAT10 resulted in robust target RNA acetylation (Fig. 5a), whereas untreated controls exhibited basal acetylation comparable to nontargeted or catalytically inactive samples.

We also designed blue-light-inducible RNA acetylation systems using the Magnet photodimerization domain[57]. pMagH and nMagH are engineered photoswitches that efficiently dimerize following blue light illumination. Fusion of dPspCas13b to nMagH and eNAT10 to pMagH triggered significant target RNA acetylation following 488-nm blue light exposure for 24 h, displaying 26-fold (NES) and 8-fold (NLS) enrichment of target RNA (Fig. 5b). Nonilluminated controls and catalytically inactive edNAT10 showed minimal acetylation signals.

To construct a small-molecule-inhibited RNA acetylation system, we used the hepatitis C virus protease NS3aH1 and ANR peptide, which bind spontaneously inside cells in the absence of a stimulus[58,59]. Treatment with the antiviral drug danoprevir renders drug-bound NS3aH1 incapable of binding to ANR, thereby abolishing the interaction between the two domains. Although not as efficient as other inducible systems, dCas13–ANR–ANR and NS3aH1–eNAT10 fusions showed target RNA acetylation signals in the absence of danoprevir that were significantly reduced by treatment with 5 μM danoprevir (Fig. 5c).

To test the reversibility of our ABA-inducible system, we treated cells with 100 μM ABA for 24 h, followed by ABA washout (Supplementary Fig. 11a). Target RNA acetylation levels started to decrease from the time of ABA withdrawal and returned to baseline 36 h after ABA washout (Supplementary Fig. 11b).

In vivo RNA acetylation with dual-AAV

To enable in vivo RNA acetylation, we developed a dual-AAV system due to size limitations of Cas13 proteins for single-AAV packaging. We split our RNA acetylation system at the linker between dCas13 and eNAT10, fused each part with split-intein fragments from the cyanobacteria *Nostoc punctiforme* (Npu)[60] and cloned them into two AAV vectors: AAV_N, carrying dCas13–NpuN, and AAV_C, carrying NpuC–eNAT10 and two gRNA cassettes. The split-intein mediates efficient covalent peptide bond formation between dCas13 and eNAT10, followed by excision of the intein fragment, recreating the original unsplit configuration of the tool. We used the cytomegalovirus (CMV) promoter and short terminator WPRE3-bGHpA[61]. For liver targeting, we chose AAV8 capsid, which predominantly transduces mouse hepatocytes following intravenous injection[61,62]. Notably, the 224-amino-acid truncation of full-length NAT10 that yielded eNAT10 enabled single-vector packaging of NpuC–eNAT10 with gRNAs, using our promoter and terminator combinations.

Retro-orbital injection of mice with AAV_N (6×10^{11} viral genomes (vg)), AAV_C (6×10^{11} vg) and mCherry-lambda2 reporter AAV (3×10^{11} vg, total dose, 1.5×10^{12} vg) resulted in successful target RNA acetylation

https://doi.org/10.1038/s41589-025-01922-3

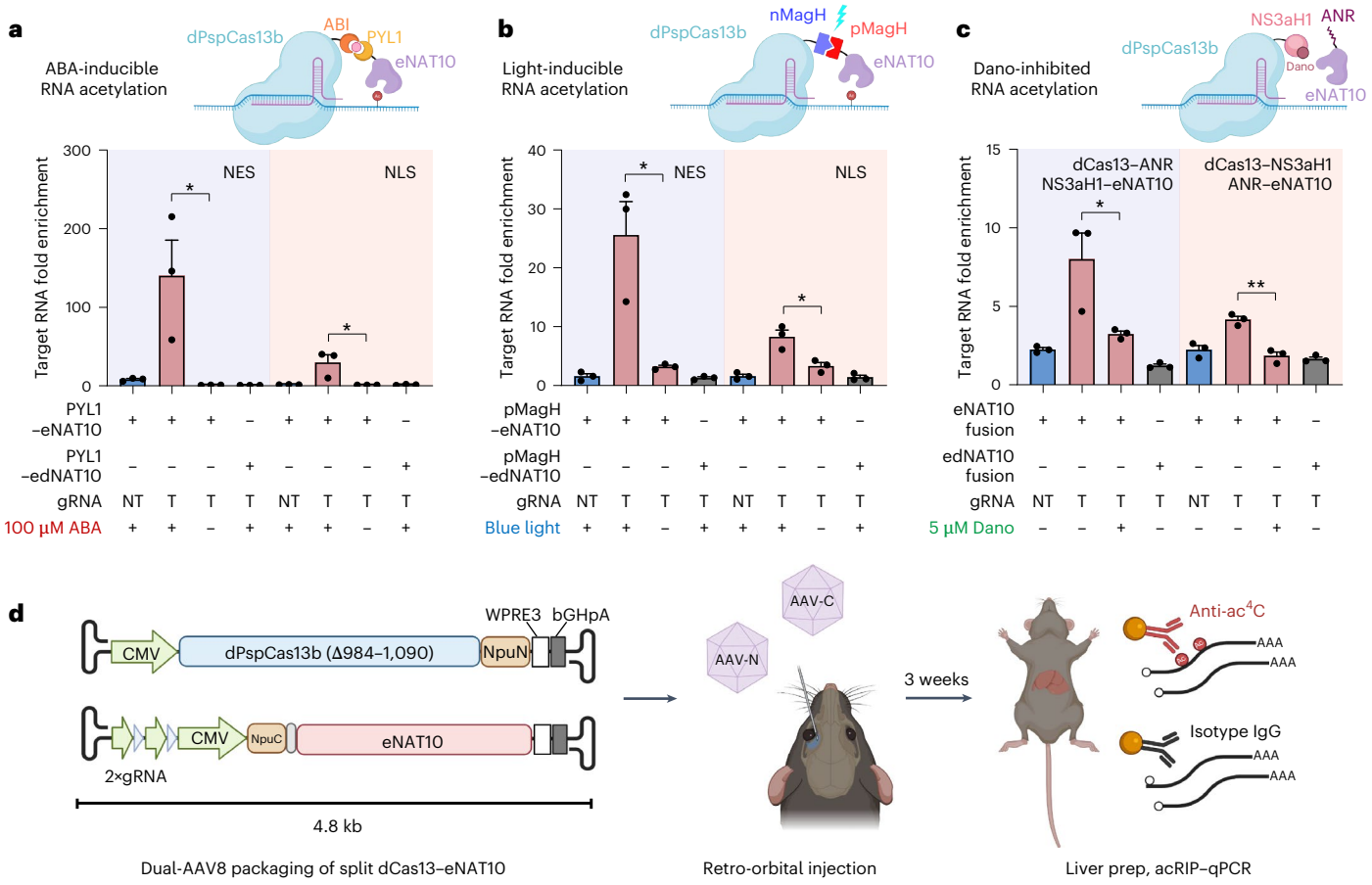

Fig. 5 | Inducible and in vivo targeted RNA acetylation. a, Small-molecule-inducible RNA acetylation system. Schematic illustration of the ABA-inducible RNA acetylation system. Top, target RNA acetylation activity with or without 24 h of 100 μM ABA treatment, measured by acRIP–qPCR. Bottom, data are presented as mean ± s.e.m. from three biologically independent replicates. Significance was calculated by two-tailed Student's *t*-test; $^{*}P < 0.05$ ($P = 3.76 \times 10^{-2}$ and 4.44×10^{-2}, from left to right). **b**, Light-inducible RNA acetylation system. Schematic illustration of the blue-light-inducible RNA acetylation system. Top, target RNA acetylation activity in the presence and absence of 488-nm blue light for 24 h, measured by acRIP–qPCR. Bottom, data are presented as mean ± s.e.m. from three biologically independent replicates. Significance was calculated by two-tailed Student's *t*-test; $^{*}P < 0.05$ ($P = 4.66 \times 10^{-2}$ and 1.85×10^{-2}, from left to right). **c**, Small-molecule-inhibited RNA acetylation system. Schematic illustration of the danoprevir (Dano)-inhibited RNA acetylation system. Top, target RNA acetylation activity with or without 24 h of 5 μM danoprevir treatment, measured by acRIP–qPCR. Only NES fusion constructs were tested. Data are presented as mean ± s.e.m. from three biologically independent replicates. Significance was calculated by two-tailed Student's *t*-test; $^{*}P < 0.05$ ($P = 4.66 \times 10^{-2}$); $^{**}P < 0.01$ ($P = 2.10 \times 10^{-3}$). **d**, Schematic illustration of AAV-mediated in vivo delivery of the target RNA acetylation system. The intein-split RNA acetylation system was packaged into AAV8 capsid and injected into C57BL/6 mice. Three weeks after injection, the bulk livers of each mouse were prepped, and reporter RNA acetylation was measured by acRIP–qPCR. **e**, Targeted exogenous mCherry-lambda2 RNA acetylation in vivo. Data are presented as mean ± s.e.m. from five (gNT and dN) or six (gT) biologically independent replicates. Significance was calculated by two-tailed Student's *t*-test; $^{**}P < 0.01$ ($P = 5.87 \times 10^{-3}$ and 4.37×10^{-3}, from left to right). **f**, Targeted endogenous *Angptl3* mRNA acetylation in vivo. Data are presented as mean ± s.e.m. from four (gT) or five (gNT and dN) biologically independent replicates. Significance was calculated by two-tailed Student's *t*-test; $^{****}P < 0.0001$ ($P = 2.40 \times 10^{-5}$ and 1.15×10^{-5}, from left to right).

in mouse liver only when lambda2 gRNA and active eNAT10 were coexpressed (Fig. 5d,e). Our promoter and terminator combinations yielded efficient expression of the AAV tool in the mouse liver (Extended Data Fig. 8a). ac^{4}C mapping by NaCNBH$_3$ RT–PCR sequencing showed increased C-to-T conversions in reporter transcripts with active eNAT10 (Extended Data Fig. 8d).

Using our dual-AAV system, we also targeted endogenous *Angptl3* (angiopoietin-like 3), which is exclusively expressed in the mouse liver[63]. We screened the efficient gRNA targeting mouse *Angptl3* and constructed a new AAV_C vector. Following retro-orbital injection of mice with dual-AAV vectors (each at a dose of 6×10^{11} vg), the endogenous *Angptl3* transcript exhibited significant degrees of acetylation only when AAV_C expressing active eNAT10 and *Angptl3*-targeting gRNA were used (Fig. 5f). Together, these results demonstrate programmable RNA chemical modification in live animals.

To assess changes in protein expression induced by targeted RNA acetylation in vivo, we performed western blotting for mCherry in liver tissue and enzyme-linked immunosorbent assays (ELISAs) for ANGPTL3 in serum samples. Both protein levels remained unchanged (Extended Data Fig. 8b,c), likely due to modest acetylation efficiency in vivo. Transcriptome-wide acRIP–seq revealed limited differential RNA acetylation (Extended Data Fig. 8e), consistent with modest acetylation efficiency observed. Additionally, LC–MS/MS analysis confirmed no significant global ac^{4}C increase in liver RNA from active eNAT10-expressing samples (Extended Data Fig. 8f).

ac^{4}C-driven RNA subcellular localization alterations

RNA modifications such as N^6-methyladenosine (m^{6}A) are known to affect transcript localization[64,65]. However, the impact of RNA acetylation on subcellular transcript localization remains unclear. To gain some evidence for the linkage between ac^{4}C modification and RNA localization, we first compared transcriptome-wide acRIP–seq data[8] to published APEX–seq[66] datasets of RNA localization across nine subcellular compartments. Surprisingly, acetylated transcripts were enriched in the cytoplasm, mitochondrial matrix and outer mitochondrial membrane and were depleted at the nuclear lamina and nucleolus (Fig. 6a and Supplementary Fig. 12a–g). Intriguingly, transcripts enriched at nuclear locations exhibited lower average ac^{4}C scores compared to depleted ones, with cytoplasm-enriched RNAs uniquely showing higher ac^{4}C scores (Fig. 6b and Supplementary Fig. 12h). Similar comparative analysis of APEX–seq results and an m^{6}A mapping dataset[67] showed distinct localization tendencies of m^{6}A-modified transcripts (Supplementary Fig. 13a–j) compared to ac^{4}C-modified transcripts.

To experimentally validate acetylation-driven RNA localization changes, we established 293T cell lines expressing APEX2 at six specific subcellular compartments (cytoplasm, nucleoplasm, nucleolus, nuclear lamina, nuclear pore and mitochondrial matrix)[66]. After confirming precise APEX2 localization (Fig. 6c), we co-transfected each cell line with mCherry-lambda2 reporter, NLS–dCas13–NLS–eNAT10 and lambda2 gRNA. Because dCas13–NES–eNAT10 can only target reporter transcripts when they finish nuclear export, we used the nuclear version of our system for this experiment. Transfected cell lines were treated with biotin-phenol and H_2O_2 for proximity-dependent RNA labeling, followed by RNA preparation, streptavidin pulldown of biotinylated RNAs and RT–qPCR analysis (APEX–qPCR; Fig. 6d).

APEX–qPCR results revealed that eNAT10-targeted reporter transcripts were more significantly enriched in the cytoplasm than catalytically inactive edNAT10-targeted reporter transcripts (Fig. 6e). Moreover, acetylated reporter RNAs were depleted from the nucleoplasm compared to unacetylated controls (Fig. 6f). Importantly, cytoplasmic and nuclear enrichment of nontargeted *ACTB* did not differ between the two sample groups (Fig. 6e,f). High specificity of proximity-dependent RNA labeling by subcellular APEX2 was further verified by enrichment level differences between mRNAs and nuclear lncRNAs (Extended Data Fig. 9a,b). In other subcellular regions, ac^{4}C-modified reporter transcripts did not show enrichment differences (Extended Data Fig. 9c–f).

To further validate these new findings in an orthogonal context, we performed nuclear–cytoplasmic fractionation of transfected 293T cells and sequenced the total RNA from each fraction (fractionation–seq). Expression level analysis of each fraction confirmed nuclear enrichment of representative nuclear RNAs and cytoplasmic enrichment of mRNAs (Extended Data Fig. 10a).

Using the NLS acRIP–seq dataset (Extended Data Fig. 5a), we identified genes that are acetylated following dCas13–eNAT10 overexpression (ac^{4}C enrichment fold change > 2). These acetylated genes exhibited a higher tendency for cytoplasmic localization in the fractionation–seq analysis of eNAT10-transfected samples than edNAT10-transfected samples (Extended Data Fig. 10b). Whereas the average cytoplasm/nucleus expression ratio of acetylated genes was 1.25 in NLS–dCas13–NLS–eNAT10 samples (median of 1.10), it dropped to 1.03 in NLS–dCas13–NLS–edNAT10 samples (median of 0.93). By contrast, unmodified RNAs with an ac^{4}C enrichment fold change of <0.5 displayed weaker cytoplasmic localization (Extended Data Fig. 10c).

Next, we extracted cytoplasm- and nucleus-enriched genes from the fractionation–seq data, defined as those with a cytoplasm/nucleus expression ratio of >2 or <0.5, respectively. Transcripts enriched in the cytoplasm exhibited significantly higher acRIP–seq ac^{4}C enrichment fold changes, with NLS–dCas13–NLS–eNAT10-transfected samples showing a larger difference between two groups (Extended Data Fig. 10d). Notably, nucleus-enriched RNAs had an average ac^{4}C enrichment fold change of 0.93 (median of 0.82) in active eNAT10-transfected samples compared to 1.00 (median of 0.86) in edNAT10-transfected samples. Cumulative distribution of ac^{4}C enrichment fold changes from NLS acRIP–seq further highlight the clear RNA acetylation differences between nucleus- and cytoplasm-enriched transcripts (Extended Data Fig. 10e,f).

Collectively, our results indicate that acetylation-prone transcripts tend to enrich more at the cytoplasm and were depleted from the nucleus, specifically following eNAT10 overexpression. These findings support our original hypothesis as well as the results from our subcellular RNA labeling experiment (Fig. 6c–f) that acetylated transcripts are more likely to localize to the cytoplasm than the nucleoplasm.

Discussion

In this study, we developed a molecular tool capable of targeting and acetylating specific transcripts of interest in living cells. Through protein engineering of human NAT10, we successfully generated a hyperactive truncation variant, termed eNAT10. Fusion of eNAT10 with RNA-binding proteins MCP and dCas13b enabled efficient acetylation of targeted exogenous and endogenous transcripts across mammalian cell lines and primary cells and in vivo, increasing protein production from acetylated RNAs.

Compared to full-length NAT10, eNAT10 was significantly more efficient when fused to dCas13 than to MCP. Although MCP has a strong interaction with MS2 stem loops ($K_d \approx 1$ nM (ref. 68)) and can bind multiple sites on the Fluc–2×MS2 reporter, dCas13 binds RNA with relatively lower affinity ($K_d \approx 10$–50 nM (refs. 23,69)) and only at a single gRNA-targeting site on the mCherry-lambda2 reporter. We postulated that nucleolar localization of dCas13–NAT10 further limits target accessibility compared to high-affinity and multibinding MCP–NAT10.

Single-base ac^{4}C mapping demonstrated that acetylation occurs broadly across targeted transcripts. Although transcript-wide acetylation effectively boosts translation efficiency, tools enabling site-specific RNA acetylation remain absent. Recently, several gRNA-only systems for site-specific A-to-I RNA editing have been reported[70–72]. More intriguingly, recent studies using engineered guide small nucleolar RNAs (gsnoRNAs) have successfully demonstrated site-specific pseudouridine installation in mammalian cells[73,74]. Notably, NAT10 is guided by the box C/D snoRNA *SNORD13* to acetylate

https://doi.org/10.1038/s41589-025-01922-3

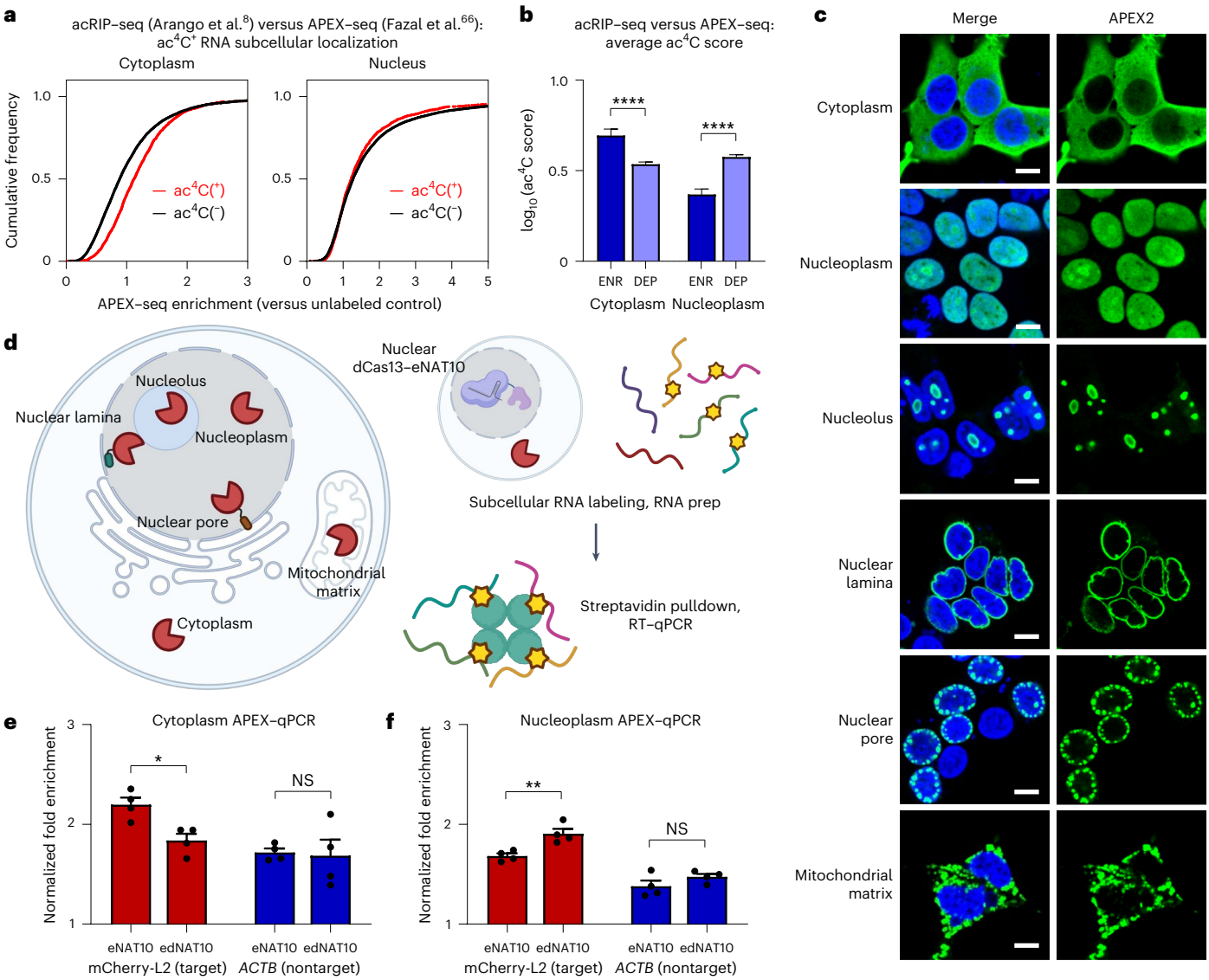

Fig. 6 | RNA acetylation can drive RNA localization alterations. **a**,**b**, Comparative analysis of APEX–seq and acRIP–seq. The list of RNAs with or without ac^4C modification and ac^4C scores of acetylated RNAs was obtained from an acRIP–seq dataset (Arango et al.[8]). A cumulative distribution plot shows differential subcellular localization of ac^4C^+ and ac^4C^- transcripts in the cytoplasm and nucleoplasm (**a**). Average ac^4C scores of transcripts enriched (ENR) and depleted (DEP) from APEX–seq are shown in **b** (subcellular RNA enrichment cutoff, $\log_2$ (fold change) > 0.75 and false discovery rate (FDR)-adjusted *P* value of <0.05; cytoplasm enriched, $n = 1{,}692$; cytoplasm depleted, $n = 10{,}934$; nucleoplasm enriched, $n = 1{,}302$; nucleoplasm depleted, $n = 11{,}287$). Significance was calculated by Mann–Whitney *U*-test; $^{****}P < 0.0001$. **c**, Subcellular localization of APEX2 fusion proteins with distinct subcellular localizations imaged after PFA fixation, permeabilization of transfected 293T cells and immunostaining of Flag tag; scale bars, 10 µm. **d**, Schematic illustration of the subcellular RNA labeling experiment with targeted RNA acetylation. The mCherry-lambda2 reporter transcript was targeted by NLS–dCas13–NLS–eNAT10. Transcripts were labeled with biotin-phenol in six different cell lines expressing APEX2 in each subcellular compartment, followed by RNA preparation, streptavidin pulldown and RT–qPCR. **e**,**f**, Subcellular enrichment of mCherry-lambda2 (target) and *ACTB* (nontarget) transcripts in the cytoplasm (**e**) and nucleoplasm (**f**), measured by streptavidin pulldown of APEX2-labeled RNA and RT–qPCR. Raw enrichment values were normalized by *GAPDH* enrichment values. Data are presented as mean ± s.e.m. from four biologically independent replicates. Significance was calculated by two-tailed Student's *t*-test; NS ($P = 8.53 \times 10^{-1}$ and 1.94×10^{-1}, from left to right); $^{*}P < 0.05$ ($P = 1.09 \times 10^{-2}$); $^{**}P < 0.01$ ($P = 7.12 \times 10^{-3}$).

RNA on the 18S rRNA helix 45 (refs. 50,75). *SNORD13*-based engineered gsnoRNAs could potentially direct specific acetylation of target residues, as suggested by a previous report[50]. However, it is important to note that endogenous NAT10 is strictly localized to the nucleolus under normal physiological conditions. This nucleolar confinement presents a challenge for using gRNA-only systems to recruit cellular NAT10 for acetylating target RNA.

Although our tool demonstrates high robustness in acetylating exogenous transcripts, its acetylation efficiency is comparatively lower when targeting endogenous transcripts. Additionally, considerable transcriptome-wide off-target RNA acetylation necessitates further engineering and optimization. Strategies to enhance the robustness and specificity of our system include using alternative dCas13 orthologs or their high-fidelity variants[76], optimizing gRNA design or using multiple guides simultaneously and further engineering eNAT10 through rational mutagenesis. These approaches may significantly improve the tool's signal-to-noise ratio, reinforcing its broad applicability across diverse research areas.

Although we have demonstrated a programmable RNA chemical modification in vivo, our AAV-delivered system showed modest efficiency, primarily due to challenges in intein-mediated protein assembly. Efficient assembly of intein-split fragments depends on

specific flanking sequences[61] and the affinity between two extein fragments. However, in our design, the dCas13–eNAT10 fusion is split at the linker region, limiting the assembly of N-extein (dCas13) and C-extein (eNAT10). Further engineering of the dual-AAV construct, particularly optimizing the intein assembly process, could improve target RNA acetylation efficiency in vivo.

Using the nuclear version of the system, we could show the cytoplasmic enrichment and nuclear depletion of ac^{4}C-modified transcripts. Interestingly, results from the comparative analysis of acRIP–seq and APEX–seq data did not perfectly correspond to our APEX–qPCR results. A lack of localization differences between acetylated and unacetylated reporter in some locations (for example, at the nuclear lamina and nucleolus) implies that our comparative analysis results may inclusively represent the localization tendencies of ac^{4}C-prone RNA species, in addition to active RNA trafficking patterns by the ac^{4}C modification itself. On the other hand, our tool provided an unprecedented opportunity to investigate the effects of RNA acetylation on transcript localization. Complementary RNA labeling methods like CAP-seq[77] could further validate these observations.

We anticipate that our tool could be applicable in diverse research settings. Cancer is an area where our tool could be used, given emerging evidence linking elevated levels of RNA acetylation with cancer progression and metastasis[7,12–15]. For instance, we demonstrated that oncogenes such as *AKT1*, *VEGFA*, *JUN* and *SOX4* can be specifically acetylated by our tool (Fig. 2c). Notably, mRNA acetylation of *AKT1* and *SOX4* has been reported as crucial for bladder cancer progression[78]. By designing dCas13 gRNAs targeting specific transcripts, researchers can investigate whether RNA acetylation of a particular gene indeed influences cancer progression.

In summary, here, we described the development of a programmable RNA acetylation system using CRISPR–Cas13. The engineered fusion protein dCas13–eNAT10 allowed robust and specific target RNA acetylation in multiple cellular contexts. We anticipate that this system will facilitate a wide range of studies focused on the discovery of novel regulatory functions of ac^{4}C in living cells. Importantly, our system offers a compelling addition to the CRISPR toolkit, potentially advancing the development of precise genome-modulating tools that use CRISPR–Cas13.

Online content

Any methods, additional references, Nature Portfolio reporting summaries, source data, extended data, supplementary information, acknowledgements, peer review information; details of author contributions and competing interests; and statements of data and code availability are available at https://doi.org/10.1038/s41589-025-01922-3.

References

1. Cappannini, A. et al. MODOMICS: a database of RNA modifications and related information. 2023 update. *Nucleic Acids Res.* **52**, D239–D244 (2024).
2. Roundtree, I. A. et al. Dynamic RNA modifications in gene expression regulation. *Cell* **169**, 1187–1200 (2017).
3. Barbieri, I. & Kouzarides, T. Role of RNA modifications in cancer. *Nat. Rev. Cancer* **20**, 303–322 (2020).
4. George, T., Gordon, J. & Rogg, H. N^4-Acetylcytidine. A previously unidentified labile component of the small subunit of eukaryotic ribosomes. *J. Biol. Chem.* **253**, 1101–1105 (1978).
5. Zachau, H. G., Dütting, B. & Feldmann, H. The structures of two serine transfer ribonucleic acids. *Hoppe Seylers Z. Physiol. Chem.* **347**, 212–235 (1966).
6. Ito, S. et al. Human NAT10 is an ATP-dependent RNA acetyltransferase responsible for N^4-acetylcytidine formation in 18S ribosomal RNA (rRNA). *J. Biol. Chem.* **289**, 35724–35730 (2014).
7. Jin, C. et al. Acetyltransferase NAT10 regulates the Wnt/β-catenin signaling pathway to promote colorectal cancer progression via ac^{4}C acetylation of KIF23 mRNA. *J. Exp. Clin. Cancer Res.* **41**, 345 (2022).
8. Arango, D. et al. Acetylation of cytidine in mRNA promotes translation efficiency. *Cell* **175**, 1872–1886 (2018).
9. Tsai, K. et al. Acetylation of cytidine residues boosts HIV-1 gene expression by increasing viral RNA stability. *Cell Host Microbe* **28**, 306–312 (2020).
10. Hao, H. et al. N^4-Acetylcytidine regulates the replication and pathogenicity of enterovirus 71. *Nucleic Acids Res.* **50**, 9339–9354 (2022).
11. Yan, Q. et al. NAT10-dependent N^4-acetylcytidine modification mediates PAN RNA stability, KSHV reactivation, and IFI16-related inflammasome activation. *Nat. Commun.* **14**, 6327 (2023).
12. Zhang, Y. et al. NAT10 promotes gastric cancer metastasis via N^4-acetylated *COL5A1*. *Signal Transduct. Target. Ther.* **6**, 173 (2021).
13. Wei, R. et al. NAT10 promotes cell proliferation by acetylating *CEP170* mRNA to enhance translation efficiency in multiple myeloma. *Acta Pharm. Sin. B* **12**, 3313–3325 (2022).
14. Zong, G. et al. NAT10-mediated AXL mRNA N4-acetylcytidine modification promotes pancreatic carcinoma progression. *Exp. Cell Res.* https://doi.org/10.1016/j.yexcr.2023.113620 (2023).
15. Liu, Y. et al. N^4-Acetylcytidine-dependent *GLMP* mRNA stabilization by NAT10 promotes head and neck squamous cell carcinoma metastasis and remodels tumor microenvironment through MAPK/ERK signaling pathway. *Cell Death Dis.* **14**, 712 (2023).
16. Zhang, M. et al. The cytidine *N*-acetyltransferase NAT10 participates in peripheral nerve injury-induced neuropathic pain by stabilizing SYT9 expression in primary sensory neurons. *J. Neurosci.* **43**, 3009–3027 (2023).
17. Xu, T. et al. Ac^{4}C enhances the translation efficiency of *Vegfa* mRNA and mediates central sensitization in spinal dorsal horn in neuropathic pain. *Adv. Sci.* **10**, 2303113 (2023).
18. Liu, R. et al. NAT10-mediated N^4-acetylcytidine mRNA modification regulates self-renewal in human embryonic stem cells. *Nucleic Acids Res.* **51**, 8514–8531 (2023).
19. Chen et al. NAT10-mediated N^4-acetylcytidine modification is required for meiosis entry and progression in male germ cells. *Nucleic Acids Res.* **50**, 10896–10913 (2022).
20. Larrieu, D. et al. Chemical inhibition of NAT10 corrects defects of laminopathic cells. *Science* **344**, 527–532 (2014).
21. Marraffini, L. A. CRISPR–Cas immunity in prokaryotes. *Nature* **526**, 55–61 (2015).
22. Heler, R. et al. Cas9 specifies functional viral targets during CRISPR–Cas adaptation. *Nature* **519**, 199–202 (2015).
23. Abudayyeh, O. O. et al. C2c2 is a single-component programmable RNA-guided RNA-targeting CRISPR effector. *Science* **353**, aaf5573 (2016).
24. Abudayyeh, O. O. et al. RNA targeting with CRISPR–Cas13. *Nature* **550**, 280–284 (2017).
25. Yang, L.-Z. et al. Dynamic imaging of RNA in living cells by CRISPR–Cas13 systems. *Mol. Cell* **76**, 981–997 (2019).
26. Cox, D. B. T. et al. RNA editing with CRISPR–Cas13. *Science* **358**, 1019–1027 (2017).
27. Abudayyeh, O. O. et al. A cytosine deaminase for programmable single-base RNA editing. *Science* **365**, 382–386 (2019).
28. Huang, X. et al. Programmable C-to-U RNA editing using the human APOBEC 3A deaminase. *EMBO J.* **39**, e104741 (2020).
29. Wilson, C. et al. Programmable m^{6}A modification of cellular RNAs with a Cas13-directed methyltransferase. *Nat. Biotechnol.* **38**, 1431–1440 (2020).

30. Li, J. et al. Targeted mRNA demethylation using an engineered dCas13b–ALKBH5 fusion protein. *Nucleic Acids Res.* **48**, 5684–5694 (2020).
31. Xia, Z. et al. Epitranscriptomic editing of the RNA N^6-methyladenosine modification by dCasRx conjugated methyltransferase and demethylase. *Nucleic Acids Res.* **49**, 7361–7374 (2021).
32. Shi, H. et al. Inducible and reversible RNA N^6-methyladenosine editing. *Nat. Commun.* **13**, 1958 (2022).
33. Han, S. et al. RNA–protein interaction mapping via MS2- or Cas13-based APEX targeting. *Proc. Natl Acad. Sci. USA* **117**, 22068–22079 (2020).
34. Yi, W. et al. CRISPR-assisted detection of RNA–protein interactions in living cells. *Nat. Methods* **17**, 685–688 (2020).
35. Otoupal, P. B. et al. CRISPR-RNAa: targeted activation of translation using dCas13 fusions to translation initiation factors. *Nucleic Acids Res.* **50**, 8986–8998 (2022).
36. Hao, M. et al. Tracking endogenous proteins based on RNA editing-mediated genetic code expansion. *Nat. Chem. Biol.* **20**, 721–731 (2024).
37. Arango, D., Sturgill, D. & Oberdoerffer, S. Immunoprecipitation and sequencing of acetylated RNA. *Bio. Protoc.* **9**, e3278 (2019).
38. Sas-Chen, A. et al. Dynamic RNA acetylation revealed by quantitative cross-evolutionary mapping. *Nature* **583**, 638–643 (2020).
39. Thalalla Gamage, S. et al. Quantitative nucleotide resolution profiling of RNA cytidine acetylation by ac^4C-seq. *Nat. Protoc.* **16**, 2286–2307 (2021).
40. Shen, Q. et al. NAT10, a nucleolar protein, localizes to the midbody and regulates cytokinesis and acetylation of microtubules. *Exp. Cell. Res.* **315**, 1653–1667 (2009).
41. Tan, Y. et al. Loss of nucleolar localization of NAT10 promotes cell migration and invasion in hepatocellular carcinoma. *Biochem. Biophys. Res. Commun.* **499**, 1032–1038 (2018).
42. Dalhat, M. et al. Structural insights of human *N*-acetyltransferase 10 and identification of its potential novel inhibitors. *Sci. Rep.* **11**, 6051 (2021).
43. Lv, J. et al. Molecular cloning of a novel human gene encoding histone acetyltransferase-like protein involved in transcriptional activation of hTERT. *Biochem. Biophys. Res. Commun.* **311**, 506–513 (2003).
44. Nelles, D. A. et al. Programmable RNA tracking in live cells with CRISPR/Cas9. *Cell* **165**, 488–496 (2016).
45. Yu, J. et al. Programmable RNA base editing with photoactivatable CRISPR–Cas13. *Nat. Commun.* **15**, 673 (2024).
46. Statello, L. et al. Gene regulation by long non-coding RNAs and its biological functions. *Nat. Rev. Mol. Cell Biol.* **22**, 96–118 (2021).
47. Leppek, K. & Stoecklin, G. An optimized streptavidin-binding RNA aptamer for purification of ribonucleoprotein complexes identifies novel ARE-binding proteins. *Nucleic Acids Res.* **42**, e13 (2014).
48. Arango, D. et al. Direct epitranscriptomic regulation of mammalian translation initiation through N^4-acetylcytidine. *Mol. Cell* **82**, 2797–2814 (2022).
49. Sturgill, D., Arango, D. & Oberdoerffer, S. Protocol for base resolution mapping of ac^4C using RedaC:T-seq. *STAR Protoc.* **3**, 101858 (2022).
50. Gamage, S. T. et al. Antisense pairing and SNORD13 structure guide RNA cytidine acetylation. *RNA* **28**, 1582–1596 (2022).
51. Beiki, H. et al. Detection of ac^4C in human mRNA is preserved upon data reassessment. *Mol. Cell* **84**, 1611–1625 (2024).
52. Yan, S. et al. Antibody-free fluorine-assisted metabolic sequencing of RNA N^4-acetylcytidine. *J. Am. Chem. Soc.* **145**, 22232–22242 (2023).
53. Relier, S. et al. Enhanced ac^4C detection in RNA via chemical reduction and cDNA synthesis with modified dNTPs. *RNA* **30**, 938–953 (2024).
54. Schiffers, S. & Oberdoerffer, S. ac^4C: a fragile modification with stabilizing functions in RNA metabolism. *RNA* **30**, 583–594 (2024).
55. Liang, F.-S., Wen, Q. H. & Crabtree, G. R. Engineering the ABA plant stress pathway for regulation of induced proximity. *Sci. Signal.* **4**, rs2 (2011).
56. Gao, Y. et al. Complex transcriptional modulation with orthogonal and inducible dCas9 regulators. *Nat. Methods* **13**, 1043–1049 (2016).
57. Kawano, F. et al. Engineered pairs of distinct photoswitches for optogenetic control of cellular proteins. *Nat. Commun.* **6**, 6256 (2015).
58. Foight, G. W. et al. Multi-input chemical control of protein dimerization for programming graded cellular responses. *Nat. Biotechnol.* **37**, 1209–1216 (2019).
59. Ding, Y. et al. Orthogonal inducible control of Cas13 circuits enables programmable RNA regulation in mammalian cells. *Nat. Commun.* **15**, 1572 (2024).
60. Iwai, H. et al. Highly efficient protein *trans*-splicing by a naturally split DnaE intein from *Nostoc punctiforme*. *FEBS Lett.* **580**, 1853–1858 (2006).
61. Davis, J. R. et al. Efficient prime editing in mouse brain, liver and heart with dual AAVs. *Nat. Biotechnol.* **42**, 253–264 (2023).
62. Gao, G.-P. et al. Novel adeno-associated viruses from rhesus monkeys as vectors for human gene therapy. *Proc. Natl Acad. Sci. USA* **99**, 11854–11859 (2002).
63. Koishi, R. et al. ANGPTL3 regulates lipid metabolism in mice. *Nat. Genet.* **30**, 151–157 (2002).
64. Roundtree, I. A. et al. YTHDC1 mediates nuclear export of N^6-methyladenosine methylated mRNAs. *eLife* **6**, e31311 (2017).
65. Merkurjev, D. et al. Synaptic N^6-methyladenosine (m^6A) epitranscriptome reveals functional partitioning of localized transcripts. *Nat. Neurosci.* **21**, 1004–1014 (2018).
66. Fazal, F. M. et al. Atlas of subcellular RNA localization revealed by APEX–seq. *Cell* **178**, 473–490 (2019).
67. Meyer, K. D. et al. Comprehensive analysis of mRNA methylation reveals enrichment in 3′ UTRs and near stop codons. *Cell* **149**, 1635–1646 (2012).
68. Tutucci, E. et al. An improved MS2 system for accurate reporting of the mRNA life cycle. *Nat. Methods* **15**, 81–89 (2018).
69. East-Seletsky, A. et al. Two distinct RNase activities of CRISPR–C2c2 enable guide-RNA processing and RNA detection. *Nature* **538**, 270–273 (2016).
70. Qu, L. et al. Programmable RNA editing by recruiting endogenous ADAR using engineered RNAs. *Nat. Biotechnol.* **37**, 1059–1069 (2019).
71. Merkle, T. et al. Precise RNA editing by recruiting endogenous ADARs with antisense oligonucleotides. *Nat. Biotechnol.* **37**, 133–138 (2019).
72. Song, J., Zhuang, Y. & Yi, C. Programmable RNA base editing via targeted modifications. *Nat. Chem. Biol.* **20**, 277–290 (2024).
73. Song, J. et al. CRISPR-free, programmable RNA pseudouridylation to suppress premature termination codons. *Mol. Cell* **83**, 139–155 (2023).
74. Luo, N. et al. Near-cognate tRNAs increase the efficiency and precision of pseudouridine-mediated readthrough of premature termination codons. *Nat. Biotechnol.* **43**, 114–123 (2025).
75. Sharma, S. et al. Yeast Kre33 and human NAT10 are conserved 18S rRNA cytosine acetyltransferases that modify tRNAs assisted by the adaptor Tan1/THUMPD1. *Nucleic Acids Res.* **43**, 2242–2258 (2015).
76. Tong, H. et al. High-fidelity Cas13 variants for targeted RNA degradation with minimal collateral effects. *Nat. Biotechnol.* **41**, 108–119 (2023).

77. Wang, P. et al. Mapping spatial transcriptome with light-activated proximity-dependent RNA labeling. *Nat. Chem. Biol.* **15**, 1110–1119 (2019).
78. Wang, G. et al. NAT10-mediated mRNA N^4-acetylcytidine modification promotes bladder cancer progression. *Clin. Transl. Med.* **12**, e738 (2022).

Methods

Ethical statement

All animal experiments in this study were conducted in accordance with the guidelines set by the Institutional Animal Care and Use Committee at the Korea Advanced Institute of Science and Technology (approval number KA2024-007-v3). All procedures adhered to the applicable institutional and national regulations.

Molecular biology

DNA fragments encoding human NAT10 and dPspCas13b were amplified from pICE-Flag-NAT10-siR-WT (Addgene, 59365) and pCMV-dCas13-M3M14nes (Addgene, 155367). DNA fragments encoding dimerization domains and split-inteins were amplified from pSLQ2817 (Addgene, 84239), nMagHigh1-EGFP-CAAX (Addgene, 67300), GWF180 (Addgene, 133607), pAAV-SMVP-Cas9N (Addgene, 80930) and pAAV-CMV-Cas9C-VPR (Addgene, 80933). DNA fragments encoding APEX2 were amplified from dCas13d-dsRBD-APEX2 (Addgene, 154939). DNA fragments encoding human SENP2 and LMNA were amplified from HEK293T cell cDNA. Point mutations and localization signals were incorporated using appropriate primers. PCR fragments were generated using Phusion High-Fidelity DNA Polymerase (Thermo Fisher) and inserted into BamHI- (New England Biolabs) and NotI-digested (New England Biolabs) pAcGFP1-N1 vector (Clontech) through Gibson assembly.

For the design of gRNAs targeting cellular transcripts, we used multiple computational tools for Cas13 guide design[79,80], as well as RNA structure prediction and binding energy analysis[81]. Candidate guides (at least three for each gene) were initially screened for their knockdown efficiency using nuclease-active PspCas13b in 293T cells and further validated for target gene acetylation efficiency with acRIP–qPCR. Plasmids encoding PspCas13b gRNA were cloned using Golden Gate Assembly. Briefly, pC0043-PspCas13b CRISPR RNA backbone (Addgene, 103854) was digested with BbsI (New England Biolabs) and ligated to annealed oligonucleotides encoding gRNA sequences. Spacer sequences used in this study are listed in Supplementary Table 1.

Following Gibson assembly or ligation, plasmids were transformed into DH5a (Yeastern Biotech) or NEB Stable (New England Biolabs) competent cells using a 1-min heat shock at 42 °C. Transformed cells were grown in a shaking incubator, recovered and spread on LB agar plates containing the appropriate antibiotics. Sixteen to 24 h after transformation, resulting colonies were inoculated into liquid LB medium containing antibiotics and incubated for 16 to 24 h. Thereafter, plasmid DNA was purified using a Plasmid DNA Purification kit (Labopass) or Nucleobond Xtra Midi EF kit (Macherey-Nagel), and cloned DNA sequences were confirmed by Sanger sequencing (Cosmogenetech).

Brief conformation of key constructs used in this study are as follows: dPspCas13b(Δ984–1090)-GS-HIVNES-XTEN-eNAT10, SV40NLS-dPspCas13b(Δ984–1090)-GS-SV40NLS-XTEN-eNAT10, dPspCas13b(Δ984–1090)-GS-HIVNES-GSG4S-ABI, HIVNES-PYL1-GS-eNAT10, dPspCas13b(Δ984–1090)-GS-HIVNES-NpuN and NpuC-XTEN-eNAT10. Protein structures were predicted using AlphaFold2 and were analyzed with PyMOL2.5.2.

Cell culture

HEK293T cells (ATCC), HeLa cells (ATCC) and N2a cells (ATCC) were cultured in DMEM (Gibco) containing 10% fetal bovine serum (FBS; Gibco) and 1% penicillin–streptomycin (Gibco). NIH3T3 cells (ATCC) were cultured in DMEM containing 10% bovine serum (Gibco). Cells were maintained in T75 flasks (SPL) at 37 °C in a humidified 10% CO_2 incubator (5% for N2a cells) and subcultured every other day.

Generation of *NAT10*-knockout HeLa cells

For knocking out endogenous *NAT10*, two CRISPR–Cas9 gRNAs targeting exon 5 of *NAT10* were designed (spacers of GTGAGTTCATGGTCCGTAGG and CTGTTTCTACAGTCCTGGCC) and cloned into pX458 (Addgene, 48138) vector expressing SpCas9 and EGFP, referring to a previous report[8]. Two gRNA plasmids were simultaneously transfected into HeLa cells at a 1:1 ratio using Lipofectamine LTX according to the manufacturer's instructions and grown for 48 h, and GFP^+ cells were sorted in singlets using MoFlo Astrios EQ (Beckman Coulter) in 96-well cell culture plates. Single colonies were expanded and genotyped by PCR amplification of collected gDNA (Genomic DNA Isolation kit, Labopass) using forward (5′-TGCATGACCAGCCCTTTCTA-3′) and reverse (5′-GCTTACCATAGTCACTGTGTACA-3′) primers and further by ac^4C mapping of 18S rRNA 1337C and 1842C.

Transfections of cell lines

For transfection of HEK293T cells for acRIP and western blotting, HEK293T cells were seeded at 5.5×10^5 cells per well in a six-well cell culture plate 1 day before transfection. Sixteen hours after seeding, cells in individual wells were transfected with 150 ng of reporter plasmid, 1,000 ng of dCas13–eNAT10 plasmid and 2,100 ng of gRNA expression plasmid (1,050 ng of each gRNA plasmid when using dual guides simultaneously) using 8.2 µg of PEI-MAX (Polysciences). For inducible systems, 293T cells were transfected with 150 ng of reporter plasmid, 650 ng each of dCas13 and eNAT10 fusion plasmids and 2,100 ng of gRNA expression plasmid using 8.8 µg of PEI-MAX. After incubating for 4 to 6 h after transfection, medium was replaced with fresh complete medium. Unless otherwise noted, transfected cells were processed for analysis 48 h after transfection. HeLa cells, N2a cells and NIH3T3 cells in six-well plates were transfected with the same amount of DNA and PEI but seeded at different densities for the transfection (HeLa, 4.5×10^5 cells per well; N2a, 7.0×10^5 cells per well; NIH3T3, 2.0×10^5 cells per well). Three wells of a six-well plate were transfected for each acRIP sample. Single wells of a six-well plate were transfected for each western blotting sample.

For flow cytometry and knockdown assays, HEK293T cells were seeded at 8.0×10^4 cells per well in a 24-well cell culture plate (SPL) 1 day before transfection. For flow cytometry, cells in a single well were transfected 16 h after seeding with 20 ng of reporter plasmid, 200 ng of dCas13–eNAT10 plasmid and 430 ng of gRNA expression plasmid using 2.1 µl of Lipofectamine LTX (Thermo Fisher) and 0.7 µl of Plus Reagent. For knockdown assays, cells were transfected with 20 ng of mouse *Angptl3* expression plasmid, 200 ng of pC0046-EF1a-PspCas13b-NES-HIV (Addgene, 103862) and 500 ng of gRNA expression plasmid. Transfected cells were processed for analysis 48 h after transfection.

For luciferase assays, HEK293T cells were seeded at 1.5×10^4 cells per well in 96-well Flat Clear Bottom Black Polystyrene Microplates (Corning). For imaging analysis, HEK293T cells were seeded at 1.5×10^4 cells per well in a poly-D-lysine-coated (Sigma) µ-Plate 96-Well Square (Ibidi). Cells were incubated for 16 h after seeding, and cells in individual wells were transfected with 10 ng of reporter plasmid, 60 ng of dCas13–eNAT10 plasmid and 130 ng of gRNA expression plasmid using 0.6 µl of Lipofectamine LTX and 0.2 µl of Plus reagent. For luciferase assays, transfected cells were processed 48 h after transfection. For imaging analysis, cells were processed 24 h after transfection.

For the ABA-inducible systems, ABA (Sigma) was reconstituted in ethanol (Merck) and added to cells at a final concentration of 100 µM 24 h after transfection. For blue-light-inducible systems, cells were illuminated with 488-nm blue light 24 h after transfection using a customized 96-well LED array (Live Cell Instruments). For danoprevir-inhibited systems, danoprevir (Apexbio) was reconstituted in dimethyl sulfoxide (Calbiochem) and added to cells at a final concentration of 5 µM 24 h after transfection. Cells were treated with ABA, blue light or danoprevir for 24 h and subsequently processed as described earlier for the corresponding experiments. For ABA washout, the medium was aspirated from transfected cells 24 h after ABA treatment, and cells were washed four times with full medium without ABA. After washout, samples were prepped at the indicated time points.

Rat primary astrocyte culture and transfection

For primary cortical astrocyte cultures, embryonic day 18 embryos were obtained from a pregnant Sprague Dawley rat (Orient Bio) killed by CO_2 inhalation, after which cortices from embryonic rat brains were dissected into HBSS (Gibco) containing 10 mM HEPES (Gibco). Trypsinized cortices were serially washed with diluted FBS in HBSS. Dissociated cells were then filtered through a 70-µm cell strainer (BD Falcon), immediately plated in T75 flasks and maintained in DMEM supplemented with 10% FBS at 37 °C in a humidified 10% CO_2 incubator. The day after plating, astrocytes were selected and retained by physically detaching other cells by tapping the culture flask, after which the medium was replaced. Cells were subcultured every other day at least four times to ensure a predominant astrocyte population.

Primary astrocytes for acRIP were transfected by first seeding cells at 2.0×10^5 cells per well in a six-well cell culture plate the day before transfection. Sixteen hours after seeding, cells in individual wells were transfected with 100 ng of reporter plasmid, 650 ng of dCas13–eNAT10 plasmid and 1,450 ng of gRNA expression plasmid using 6.6 µl of GeneJuice Transfection Reagent (Sigma). Six hours after transfection, the medium was replaced with fresh medium, and transfected cells were incubated for 48 h before processing for analysis.

RNA isolation and RT–qPCR

Cells were detached from the plate using trypsin-EDTA (Gibco) and washed once with DPBS (Gibco). Total RNA was isolated and purified using a PureLink RNA Mini kit (Invitrogen), according to the manufacturer's protocol. Purified or immunoprecipitated RNA was reverse transcribed using a PrimeScript RT reagent kit with gDNA Eraser (Takara), according to manufacturer's protocol. Reverse transcription was performed at 37 °C, unless otherwise noted. Synthesized cDNA was processed for qPCR using synthesized cDNA, gene-specific primers (Supplementary Table 2) and SYBR Green Realtime PCR Master Mix (Toyobo). Human *GAPDH* and mouse and rat *Gapdh* were used as reference genes for cycling threshold (C_q) value normalization for the corresponding RNA samples. All qPCR reactions were performed on a CFX Opus 96 Real-Time PCR system (Bio-Rad).

acRIP–qPCR

The procedure used for acRIP experiments is a modification of the original protocol[8,37] that incorporates published RNA immunoprecipitation protocols[29,82]. One day before immunoprecipitation, 30 µl of Protein G Dynabeads (Invitrogen) per reaction was mixed with antibody and incubated overnight at 4 °C with rotation. For immunoprecipitated samples, 1.5 µg of rabbit anti-ac4C (Abcam, ab252215) was used for each sample; control samples used 1.5 µg of rabbit isotype IgG (Cell Signaling Technology, 3900). In both cases (anti-ac4C and isotype controls), 35 µg of isolated total RNA was mixed with antibody-conjugated beads. After adjusting the total incubation volume to 300 µl with RIP buffer (10 mM Tris-HCl pH 7.4 and 150 mM NaCl in distilled water, Biosolution) containing 0.1% (vol/vol) mouse RNase inhibitor (New England Biolabs) and 0.3% (vol/vol) IGEPAL CA-630 (Sigma), samples were incubated for 4 h at 4 °C with rotation. After incubation, beads were washed three times with 500 µl of RIP buffer, and bound RNA was eluted using 100 µl of lysis buffer provided in the PureLink RNA Mini kit, supplemented with 1% β-mercaptoethanol (Sigma). Eluted RNA was purified using an RNA Clean & Concentrator kit (Zymo Research), according to manufacturer's protocol. A total of 20 µl of RNase-free distilled water (Gibco) was used for eluting purified RNA.

Immunoprecipitated, purified RNA was processed for qPCR analysis as described above. C_q values of target RNA were initially normalized to those of *GAPDH*, after which fold enrichment of target RNA was calculated by dividing normalized C_q values of anti-ac^{4}C samples with normalized C_q values of the corresponding isotype control samples.

Western blotting

Transfected cells were washed once with DPBS and detached from the plate with cell scrapers (Sarstedt). Cells were lysed, and cellular proteins were purified using PRO-PREP (Intron Biotechnology). After measuring protein concentration, 25 µg (for 15-well gels) or 35 µg (for 10-well gels) of total protein was mixed with 5× SDS–PAGE loading buffer (Biosesang), denatured at 95 °C for 5 min and loaded onto Bolt 4–12% Bis-Tris protein gels (Invitrogen) with Precision Plus Protein All Blue Standards (Bio-Rad). Resolved proteins were transferred to a nitrocellulose membrane (Invitrogen) using an iBlot 3 Western Blot Transfer System (Thermo Fisher).

After blocking by incubation with Intercept TBS Blocking Buffer (LI-COR) for 1 h at room temperature, membranes were incubated with primary antibody (in blocking buffer) overnight at 4 °C. Rabbit anti-DYKDDDDK tag (1:1,000; Cell Signaling Technology, 14793), mouse anti-FUS (1:1,000; Abcam, ab283272), rabbit anti-PTEN (1:5,000; Abcam, ab32199), rat anti-mCherry (1:1,000; Invitrogen, M11217), mouse anti-GAPDH (1:5,000; Invitrogen, MA5-15738) and rabbit anti-β-actin (1:1,000; Cell Signaling Technology, 4970) were used as primary antibodies. Membranes were washed three times with 0.1% Tween-20 (Sigma) in TBS (Welgene) and incubated with secondary antibodies in blocking buffer for 1 h at room temperature. IRDye 680RD-conjugated donkey anti-rabbit (1:10,000; LI-COR, 926-68073), IRDye 800CW-conjugated donkey anti-rabbit (1:10,000; LI-COR, 926-32213), IRDye 680RD-conjugated donkey anti-mouse (1:10,000; LI-COR, 926-68072), IRDye 800CW-conjugated goat anti-rat (1:10,000; LI-COR, 926-32219) and IRDye 800CW-conjugated donkey anti-mouse (1:10,000; LI-COR, 926-32212) were used as secondary antibodies. Membranes were again washed three times with 0.1% Tween-20 in TBS and imaged using an Odyssey CLx imaging system and Image Studio v5.2. Bands were quantified densitometrically using ImageJ v5.2.

Immunocytochemistry

Transfected cells were fixed by incubating with 4% PFA (Electron Microscopy Sciences) for 15 min at room temperature. Cells were then washed three times with DPBS containing 0.1% Tween-20 (Sigma) and permeabilized with DPBS containing 0.1% Triton X-100 (Sigma) for 15 min at room temperature. After an additional three washes with DPBS containing 0.1% Tween-20, cells were blocked by incubating with DPBS containing 3% bovine serum albumin (BSA; Sigma) for 1 h at room temperature. Cells were then incubated overnight at 4 °C with primary antibodies diluted in DPBS containing 1% BSA. Rabbit anti-DYKDDDDK tag (1:700; Cell Signaling Technology, 14793), rat anti-DYKDDDDK tag (1:700; BioLegend, 637301) and rabbit anti-acetyl lysine (1:700; Abcam, ab80178) were used as primary antibodies. Cells were then incubated with secondary antibodies diluted in DPBS containing 1% BSA and the nuclear stain Hoechst 33342 (Life Technology) for 1 h at room temperature in the dark. Alexa Fluor 488-conjugated goat anti-rabbit (1:1,000; Thermo Fisher, A11034), Alexa Fluor 594-conjugated goat anti-rabbit (1:1,000; Thermo Fisher, A11037) and Alexa Fluor 488-conjugated goat anti-rat (1:1,000; Thermo Fisher, A11006) were used as secondary antibodies. After washing three times with DPBS containing 0.1% Tween-20, stained cells were imaged using confocal microscopy.

Confocal microscopy

Live cells and stained cells were imaged under a confocal microscope. Imaging was performed using a Nikon A1R confocal microscope mounted onto a Nikon Eclipse Ti body equipped with a Nikon CFI Plan Apochromat VC objective (×60/1.4-NA) and a Chamlide TC system for maintaining environmental conditions (37 °C and 10% CO_2; Live Cell Instruments).

Flow cytometry

Transfected cells were trypsinized and washed two times with flow buffer (DPBS containing 1% BSA). Cells were resuspended in flow buffer,

and flow cytometry analyses were conducted using an LSRFortessa cell analyzer (BD Biosciences). Single, live cells were gated based on forward scatter (FSC) and side scatter (SSC) values. The fluorescence of each cell was measured and analyzed with FlowJo v10. For quantification of relative protein expression, mCherry fluorescence was normalized to that of control EBFP2 fluorescence.

Luciferase assay

Luciferase assays were performed using a Dual-Glo Luciferase Assay System (Promega). Briefly, after aspirating the medium from transfected cells, 150 µl of a 1:1 mixture of Dual-Glo Luciferase Assay Reagent and DBPS was added to each well of transfected cells and incubated for 20 min at room temperature. Firefly luminescence was then measured using a Spark Microplate Reader (Tecan). Thereafter, 75 µl of Stop & Glo Buffer containing *Renilla* luciferase substrate was added to each well, and plates were incubated for 50 min at room temperature. *Renilla* luminescence was measured with a microplate reader, and relative protein expression was determined by normalizing firefly luminescence to control *Renilla* luminescence.

acRIP–seq

HEK293T cells were transfected with mCherry-lambda2 reporter, dCas13–eNAT10 and gRNA as described above. Total RNA was isolated, immunoprecipitated and purified as described in 'Acetylated RNA immunoprecipitation and quantitative PCR'. The sequencing library was constructed from purified total RNA using a SureSelect RNA Direct kit (Agilent), as described by the manufacturer. Briefly, total RNA was first fragmented into small pieces, and cleaved RNA fragments were copied into first-strand cDNA using random primers, followed by second-strand cDNA synthesis. A single 'A' base and adaptors were ligated to cDNA fragments. The products were then purified and enriched by PCR to create the cDNA library.

A SureSelect XT Human All Exon V6+UTRs kit (Agilent) was used for the capture and amplification of human exonic regions. Briefly, 250 ng of cDNA library was mixed with hybridization buffers, blocking mixes, RNase blockers and 5 µl of the SureSelect All Exon Capture Library reagent. The capture library was then washed and subjected to a second round of PCR amplification. The final purified product was quantified using Library Quantification kits for Illumina Sequencing platforms according to the qPCR Quantification Protocol Guide (Kapa Biosystems), and its quality was assessed using a TapeStation D1000 ScreenTape (Agilent). Paired-end (2 × 100 base pair) sequencing of indexed libraries was performed by Macrogen using an Illumina NovaSeq system.

Raw reads were trimmed using Trimmomatic v0.40 (settings: 3 leading/trailing; 4:15 sliding window; 36 minlen), and trimmed reads were aligned and quantified to the RefSeq GRCh38 human transcriptome or RefSeq GRCm39 mouse transcriptome using Kallisto (v.0.43.1). Subsequently, an expression matrix was obtained, and the transcript ID was matched with each annotated gene name using tximport (v.1.22.0), with RefSeq GFF as a reference. TPM values of transcripts were initially normalized to TPM values of *GAPDH*. Fold enrichment of each transcript was then calculated by dividing normalized TPM values of anti-ac^{4}C samples with normalized TPM values of corresponding isotype control samples. Differential RNA acetylation analysis was performed using unpaired *t*-tests with FDR correction.

From the NES acRIP–seq results, 13 highly acetylated and highly expressed genes in 293T cells were specified for further analysis, using the following criteria: average TPM of >300, NES acRIP–seq average fold change of >10 (compared to edNAT10-transfected samples) and adjusted *P* value of <0.05.

Total RNA sequencing

HEK293T cells were transfected with dCas13–eNAT10 or dCas13-edNAT10, lambda2 gRNA and mCherry-lambda2 reporter, as described above. Purified total RNA was used in sequencing library construction, exome capture and sequencing procedures, as described in 'Acetylated RNA immunoprecipitation and sequencing'. Raw reads were trimmed using Trimmomatic v0.40, and trimmed reads were aligned and quantified to the RefSeq GRCh38 human transcriptome using Kallisto (v.0.43.1). Subsequently, an expression matrix was obtained, and each transcript ID was matched with each annotated gene name using tximport (v.1.22.0), with RefSeq GRCh38 GFF as a reference. The expression level of each transcript was calculated as TPM, and differential transcript expression was analyzed by unpaired *t*-tests with FDR correction.

Single-base-resolution mapping of ac^{4}C and ac^{4}C sequencing

The protocol for single-base-resolution mapping of ac^{4}C is a modification of the original protocol[36,37], with reference to another similar protocol[46,47]. Total RNA purified from untransfected 293T cells was used for protocol optimization. For mapping ac^{4}C residues in reporter RNA, total RNA samples from transfected HEK293T cells were immunoprecipitated and purified using the acRIP protocol described above. Eluted RNA was split into two reactions. The first half (10 µl) was incubated with 10 µl of 1 M $NaCNBH_3$ (Sigma) and 10 µl of 1 M HCl (Sigma), and the reaction volume was adjusted to 100 µl with nuclease-free distilled water. The second half ($NaCNBH_3$-untreated controls) was the same except that $NaCNBH_3$ was replaced with 10 µl of distilled water. Reactions were performed for 20 min at room temperature and were terminated by the addition of 30 µl of Tris-HCl pH 8.0 (LPS solution). RNA was precipitated with 3 M sodium acetate (Invitrogen) and 70% ethanol.

Precipitated RNA was resuspended in nuclease-free distilled water and reverse transcribed using a PrimeScript RT reagent kit with gDNA Eraser, as described in 'RNA isolation and quantitative PCR with reverse transcription'. The reverse transcription temperature was adjusted to 42 °C because this temperature yielded modestly increased C-to-T conversion rates of acetylated cytidines compared to the default temperature of 37 °C. cDNA was PCR amplified using reporter gene-specific primers or 18S rRNA-specific primers and gel purified to ensure specific amplification. Single-end (1 × 100 base pair) sequencing of amplified cDNA using an Illumina MiSeq system was conducted by Bionics. The C-to-T conversion ratio was analyzed for all cytidine residues with mapped reads. Sequence logos of ac^{4}C-modified residues were created using WebLogo software (https://weblogo.berkeley.edu/logo.cgi). Twenty-one-nucleotide sequences flanking C-to-T-converted bases were analyzed, and a 7-nucleotide-long sequence logo was created.

For transcriptome-wide ac^{4}C-seq, precipitated RNA was resuspended in nuclease-free distilled water and subjected to sequencing library construction and cDNA synthesis using a SureSelect RNA Direct kit and SureSelect XT Human All Exon V6+UTRs kit, as described in 'Acetylated RNA immunoprecipitation and sequencing'. ac^{4}C-seq results were analyzed referring to a previous report[48]. Briefly, raw reads were trimmed using Trimmomatic v0.40, and trimmed reads were aligned to the reference human genome GRCh38 using HISAT2, with 6-nucleotide trimming at both ends of the read. Aligned reads were filtered to exclude unmapped reads, secondary alignments, duplicated reads and supplementary alignments, followed by extraction of read counts at each position using the samtools mpileup command. Results were tabulated using VarScan v.2.3.9 and further analyzed using custom Python code. Browser shots of sequenced reads were obtained from IGV v.2.17.4 software.

Sanger sequencing analysis of C-to-T conversion was conducted using the open-source Sanger chromatogram analysis tool Indigo (https://www.gear-genomics.com/indigo/), with input ab1 files. Sanger mismatch rates were determined by first extracting the peak height of C and T at each position with Indigo, followed by calculating $T / (C + T) \times 100$.

Quantification of ac^{4}C by liquid chromatography–tandem mass spectrometry

Total RNA was extracted as described in 'RNA isolation and quantitative PCR with reverse transcription'. For the enrichment of target mCherry-lambda2–4×S1m reporter from total RNA samples, 50 µg of total RNA purified from reporter- and tool-transfected 293T cells was incubated with Pierce Streptavidin Magnetic Beads (Invitrogen) in 300 µl of IPP buffer (Biosolution) containing 0.1% (vol/vol) mouse RNase inhibitor. Samples were incubated for 2 h at 4 °C with rotation. After incubation, beads were washed three times with 500 µl of B&W buffer (5 mM Tris-HCl pH 7.5, 0.5 mM EDTA, 1 M NaCl and 0.1% Tween-20), and bound RNA was eluted using 100 µl of lysis buffer provided in the PureLink RNA Mini kit, supplemented with 1% β-mercaptoethanol. Eluted RNA was purified using an RNA Clean & Concentrator kit, according to manufacturer's protocol. For the enrichment of poly(A) RNA, a Dynabeads mRNA Purification kit (Invitrogen) was used following the manufacturer's protocol. For the isolation of the small RNA fraction, a mirVana miRNA isolation kit (Invitrogen) was used following the manufacturer's protocol.

For the streptavidin-enriched target RNA samples, whole eluted samples were subjected to digestion. Otherwise, 1 µg of eluted and enriched RNA was subjected to digestion using Nucleoside Digestion Mix (New England Biolabs) as per the manufacturer's instructions, followed by dilution of the sample in 100 µl of nuclease-free distilled water. For the quantification of unmodified cytosine, samples were further diluted ten times to prevent saturation. Ten microliters of each sample was analyzed using a HPLC Triple Quadrupole Mass Spectrometer (LCMS-8050, Shimadzu) with a Hypersil Gold C18 column (Thermo Fisher). ac^{4}C and unmodified cytosine were quantified according to the standard running at the same batch, and the ac^{4}C/C ratio was calculated.

Quantitative whole-proteome analysis

Whole-proteome analysis was performed similar to as described in a previous report[73] with adjustments. Briefly, dCas13–NES–eNAT10-transfected 293T cells were collected, lysed with 5% SDS (Invitrogen) and 50 mM triethylammonium bicarbonate buffer pH 8.5 (Sigma) and treated with Benzonase (Sigma). After clearing debris by centrifugation, the protein concentration was adjusted to 300 µg in 46 µl, and samples were subjected to reduction, alkylation, digestion and purification with an S-trap kit (PROTIFI) in the KAIST Analysis Center for Research Advancement. Digested peptide was dissolved in 0.1% formic acid in distilled water and quantified, and the concentration was adjusted to 1 µg µl^{-1}. Two micrograms of peptide was used for MS analysis using an Orbitrap Eclipse mass spectrometer (Thermo Fisher). Raw data were processed with Proteome Discoverer 2.2, and subsequent analysis was performed as described previously[73]. Relative differences in protein expression levels between two sample groups were calculated.

AAV production and purification

HEK293T cells were seeded onto 150-mm cell culture plates (SPL) in DMEM supplemented with 10% FBS. When cells reached 80–90% confluency, they were transfected with 4.15 µg of transfer plasmid, 8.3 µg of helper plasmid and 16.6 µg of AAV8 rep-cap plasmid per plate using 48 µg of PEI-MAX. After incubating for 6 h, the medium was replaced with fresh medium. Three days after transfection, medium containing AAV was removed from the cell cultures, prepped and stored at 4 °C, and fresh medium was added to the plates. Five days after transfection, medium was prepared, cells were collected using cell scrapers, and collected medium and cells were processed for AAV purification.

AAV was purified according to a previously published protocol[83]. Briefly, cells were pelleted and incubated with salt-activated nuclease (ArcticZymes Technologies). AAV particles in the culture medium were precipitated using polyethylene glycol 8000 (Sigma) at a final concentration of 8%. The mixture of precipitated viral particles and cell supernatant was centrifuged through OptiPrep (Serumwerk) iodixanol gradients of 15, 25, 40 and 60%. AAV particles were further purified by washing with DPBS followed by centrifugation in a 100-kDa Amicon filter device (Millipore). The titer of purified AAV was measured using an AAVpro Titration kit (Takara), according to the manufacturer's protocol.

AAV injection and hepatic RNA isolation

For in vivo experiments, 4- to 5-week-old male B6SJL mice (Raonbio) were allowed to acclimate for 1 week before injection. All mice were housed under a 12-h light/12-dark cycle at room temperature and 40% humidity. After anesthetizing with 2,2,2-tribromoethanol (Sigma), mice were injected with a total volume of AAV (adjusted with DPBS) of 100 µl per mouse. For exogenous reporter RNA acetylation experiments, 5- to 6-week-old B6SJL mice were retro-orbitally injected with 6×10^{11} vg (AAV_N virus), 6×10^{11} vg (AAV_C virus) and 3×10^{11} vg (target reporter virus; total AAV dose, 1.5×10^{12} vg). For endogenous reporter RNA acetylation experiments, 5- to 6-week-old B6SJL mice were retro-orbitally injected with 6×10^{11} vg (AAV_N virus) and 6×10^{11} vg (AAV_C virus; total AAV dose, 1.2×10^{12} vg). No injected mice showed apparent behavioral abnormalities before the experimental end point.

Three weeks after injection, mice were killed, and bulk livers were immediately prepared. Liver tissues from a single mouse were homogenized and lysed in 25 ml of lysis buffer from a PureLink RNA Mini kit using a 50-ml syringe and 18-gauge needles (Kovax). Samples were briefly centrifuged, and the supernatant was processed for RNA purification and acRIP–qPCR as described above.

ANGPTL3 ELISA

Blood was collected from mice in heparin-coated tubes (MEDICALSK) via submandibular bleeding 3 weeks after AAV injection. Plasma was isolated by centrifuging blood samples at 2,000*g* for 10 min at 4 °C and immediately stored at −80 °C until use. ANGPTL3 levels were measured using a Quantikine Mouse Angiopoietin-Like 3 ELISA kit (R&D Systems), following the manufacturer's instructions. Optical density was recorded using a Spark Microplate Reader with a wavelength correction at 570 nm.

Comparative analysis of APEX–seq, acRIP–seq and methylated RNA immunoprecipitation and sequencing

Subcellular enrichment of each transcript from APEX–seq data[66] was analyzed with the acRIP–seq dataset[8]. For the generation of a cumulative distribution plot, we compared APEX–seq enrichment ratios at each subcellular compartment between acetylated and nonacetylated transcripts. To compare the average ac^{4}C scores (adopted from the acRIP–seq dataset) of transcripts enriched and depleted from each subcellular region, we obtained cutoffs of $\log_2$ (enrichment fold change) of >0.75 and an FDR-adjusted *P* value of <0.05, as described in the APEX–seq paper. Comparative analysis of APEX–seq and methylated RNA immunoprecipitation and sequencing[67] data was performed in a similar manner, except that we compared average m^{6}A counts per transcript enriched and depleted from each subcellular region.

Proximity-dependent RNA labeling with APEX2

APEX2 expression plasmids with localization tags were cloned as previously described[66,84]. HEK293T cells were transfected with lentiviral packaging plasmids and APEX2 expression plasmids, and the lentiviral supernatant was mixed with polybrene (8 µg ml^{-1}; Sigma) and transferred to newly seeded HEK293T cells for the transduction. Transduced cells were selected with 5 µg ml^{-1} blasticidin (Gibco) for at least three passages.

Cell lines stably expressing APEX2 at each subcellular region were seeded onto 100-mm cell culture plates (SPL) in DMEM supplemented with 10% FBS. When cells reached 80–90% confluency, they were

transfected with 0.9 µg of reporter plasmid, 5.4 µg of dCas13–NES–eNAT10 (or edNAT10) plasmid and 11.7 µg of lambda2 gRNA plasmid per plate using 40 µg of PEI-MAX. After incubating for 4 h, the medium was replaced with fresh medium. Two days after transfection, APEX labeling was performed as previously described[73]. Briefly, cells were treated with 500 µM biotin-phenol (Sigma) for 30 min in a 37 °C CO_2 incubator. H_2O_2 (1 mM; Sigma) was added to cells in the presence of biotin-phenol, and the plates were gently agitated for 1 min at room temperature. For unlabeled control samples, the H_2O_2 treatment was skipped. The reaction was quenched using quenching buffer containing 10 mM sodium azide (Sigma), 10 mM sodium ascorbate (Sigma) and 5 mM Trolox (Sigma). Cells were scraped, and total RNA was purified using a Labopass RNA mini kit (Cosmogenetech) with DNase treatment.

For the enrichment of biotinylated RNAs, 15 µl of Pierce Streptavidin Magnetic Beads for each sample was washed twice with B&W buffer and IPP buffer. Beads were mixed with 35 µg of purified RNA for each sample, and the volume was adjusted to 300 µl with IPP buffer. Three microliters of mouse RNase inhibitor was added for each sample, and the mixture was incubated at 4 °C for 2 h with rotation. After incubation, beads were washed three times with 500 µl of B&W buffer, and bound RNA was eluted by incubation with Proteinase K (Invitrogen) at 42 °C for 1 h and then at 55 °C for 30 min. Eluted RNA was purified, reverse transcribed and analyzed by qPCR, as described above. Relative enrichment of target RNA was calculated by dividing C_q values of target RNA in labeled samples by those of unlabeled control samples. Normalized fold enrichment of target RNA was calculated by dividing relative enrichment of target RNA by relative enrichment values of the corresponding *GAPDH* RNA.

Fractionation sequencing

Nuclear–cytoplasmic fractionation was performed using 293T cells transfected with the nuclear version of the tool. Briefly, transfected cells grown in six-well cell culture plates were collected and resuspended in 200 µl of lysis buffer (10 mM Tris-HCl pH 7.4, 10 mM NaCl, 3 mM $MgCl_2$ and 0.1% IGEPAL CA-630 in DPBS). Cells were lysed on ice for exactly 2 min, and the lysis was terminated by adding 500 µl of resuspension buffer (1% BSA, 0.2 U $µl^{-1}$ mouse RNase inhibitor in DPBS). Samples were centrifuged at 500*g* for 10 min at 4 °C, and the supernatant was carefully collected for the cytoplasmic fraction. Pellets were washed two more times with 500 µl of resuspension buffer, and the resulting pellet was collected to obtain the nuclear fraction. The cytoplasmic and nuclear fractions were subjected to RNA isolation and total RNA sequencing as described in 'Total RNA sequencing'.

Statistics and reproducibility

All representative images are from two independent experiments. All representative blots are from two or three independent biological replicates. Data are presented as mean ± s.e.m. The numbers of replicates for each experiment are indicated in the figure legends. The significance of differences between two sample means was calculated by two-tailed Student's *t*-test, one-way analysis of variance or Mann–Whitney *U*-test. Statistical analyses and data plotting were performed using GraphPad Prism 9 and Microsoft Excel for Microsoft 365 (version 2503).

Reporting summary

Further information on research design is available in the Nature Portfolio Reporting Summary linked to this article.

Data availability

The RNA-seq, acRIP–seq, ac^4C-seq and fractionation–seq data generated in this study are deposited in the NCBI Gene Expression Omnibus under accession number GSE293920. The hg38 (GRCh38.p14) and mm39 (GRCm39) reference genomes were used for RNA-seq alignment in HEK293T cells and mouse tissues. Source data are provided with this paper.

References

79. Labun, K. et al. CHOPCHOP v3: expanding the CRISPR web toolbox beyond genome editing. *Nucleic Acids Res.* **47**, W171–W174 (2019).
80. Wei, J. et al. Deep learning and CRISPR–Cas13d ortholog discovery for optimized RNA targeting. *Cell Syst.* **14**, 1087–1102 (2023).
81. Gruber, A. R. et al. The vienna RNA websuite. *Nucleic Acids Res.* **36**, W70–W74 (2008).
82. Dominissini, D. et al. Transcriptome-wide mapping of N^6-methyladenosine by m^6A-seq based on immunocapturing and massively parallel sequencing. *Nat. Protoc.* **8**, 176–189 (2013).
83. Challis, R. C. et al. Systemic AAV vectors for widespread and targeted gene delivery in rodents. *Nat. Protoc.* **14**, 379–414 (2019).
84. Kaewsapsak, P. et al. Live-cell mapping of organelle-associated RNAs via proximity biotinylation combined with protein–RNA crosslinking. *eLife* **6**, e29224 (2017).

Acknowledgements

This work was supported by Samsung Science and Technology Foundation (SSTF-BA1902-06 to W.D.H.), the Bio&Medical Technology Development Program of the National Research Foundation (NRF) funded by the Korean government (RS-2023-00263628 to W.D.H.) and NRF grants RS-2024-00440778 and RS-2024-00332454 (to K.-J.Y.). J.Y. was in part supported by Merck International Graduate Fellowship.

Author contributions

J.Y. and W.D.H. conceptualized the study and designed the experiments. J.Y., J.J., E.K. and H.J. performed most of the experiments. C.K. assisted with AAV production and isolation. S.S. conducted primary rat astrocyte culture. J.Y. performed formal data analysis. J.Y., S.-k.C. and D.K. analyzed the sequencing data. K.-J.Y. and W.D.H. supervised the project. J.Y. and W.D.H. wrote the manuscript with valuable input from all authors. J.Y., J.J. and W.D.H. revised the manuscript.

Competing interests

J.Y. and W.D.H. have filed patent applications on aspects of this work.

Additional information

Extended data is available for this paper at https://doi.org/10.1038/s41589-025-01922-3.

Supplementary information The online version contains supplementary material available at https://doi.org/10.1038/s41589-025-01922-3.

Correspondence and requests for materials should be addressed to Won Do Heo.

Peer review information *Nature Chemical Biology* thanks Yang Li and the other, anonymous, reviewer(s) for their contribution to the peer review of this work.

https://doi.org/10.1038/s41589-025-01922-3

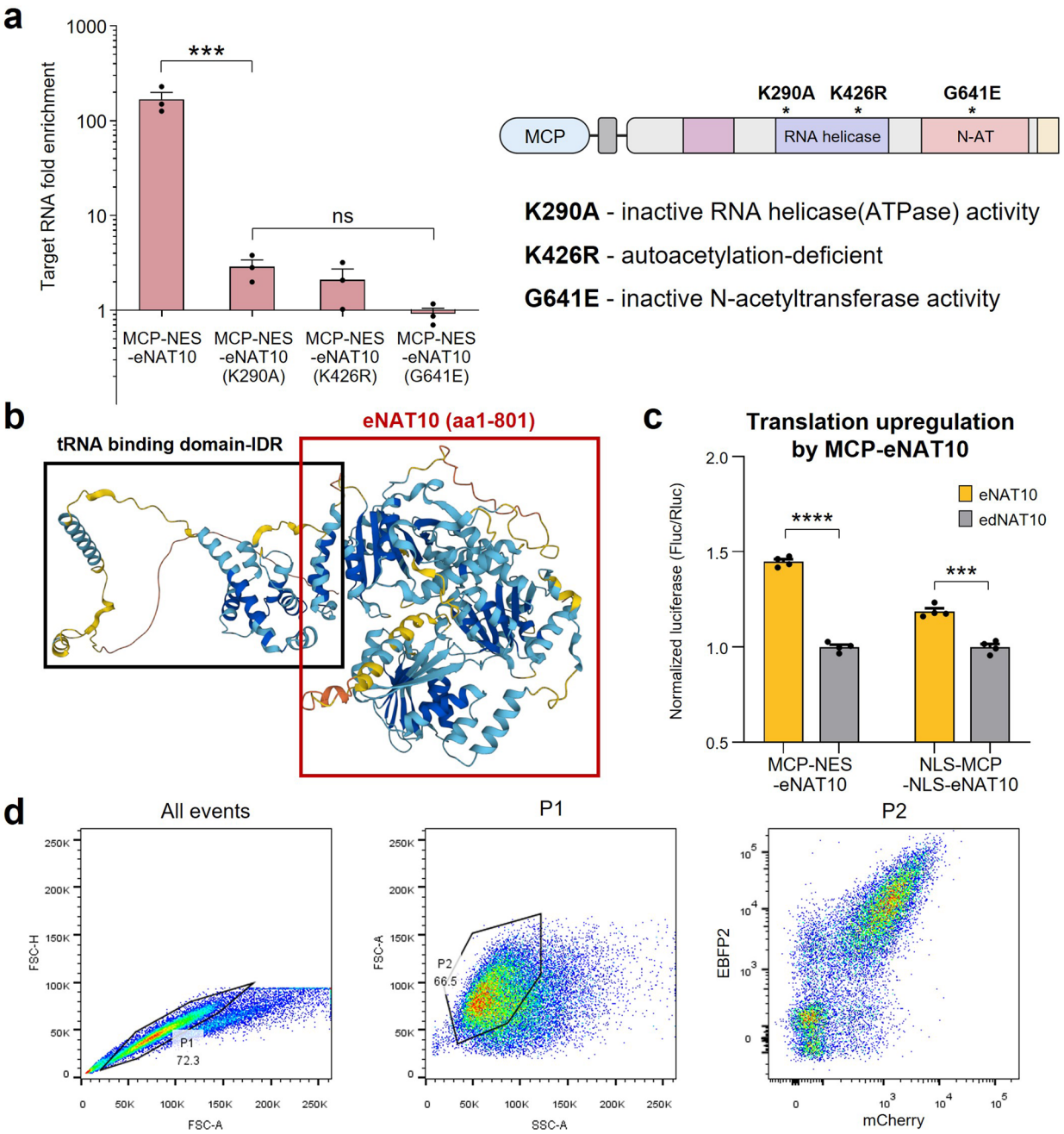

Extended Data Fig. 1 | Characterization of eNAT10, robust RNA acetyltransferase. a, Target RNA acetylation activity of MCP-fused eNAT10 mutants, measured by acRIP-qPCR. acRIP signal of each mutant (left) and description of each mutated residue (right). Data are presented as the mean ± s.e.m. from three biologically independent replicates. Significance was calculated by one-way ANOVA. ns (P = 1.00); ***P < 0.001 ($P = 4.00 \times 10^{-4}$). **b**, Predicted structure of full-length NAT10 by AlphaFold2. eNAT10 residue is depicted in red box. **c**, Translation upregulation by luciferase reporter mRNA acetylation in 293T cells. 2xMS2-fused firefly luciferase mRNA was targeted by NES or NLS-fused MCP-eNAT10. Firefly luciferase signal was normalized to expression control Renilla luciferase signal. Data are presented as the mean ± s.e.m. from four biologically independent replicates. Significance was calculated by two-tailed Student's t-test. ***P < 0.001 ($P = 1.83 \times 10^{-4}$); ****P < 0.0001 ($P = 3.22 \times 10^{-7}$). **d**, Gating strategy for flow cytometry analysis in Fig. 1f. Singlets were identified by gating FSC-H vs FSC-A (P1). Intact cells were then gated based on FSC-A vs SSC-A for appropriate size and granularity (P2). Mean fluorescence intensities of EBFP2 and mCherry were analyzed from cells gated in P2.

https://doi.org/10.1038/s41589-025-01922-3

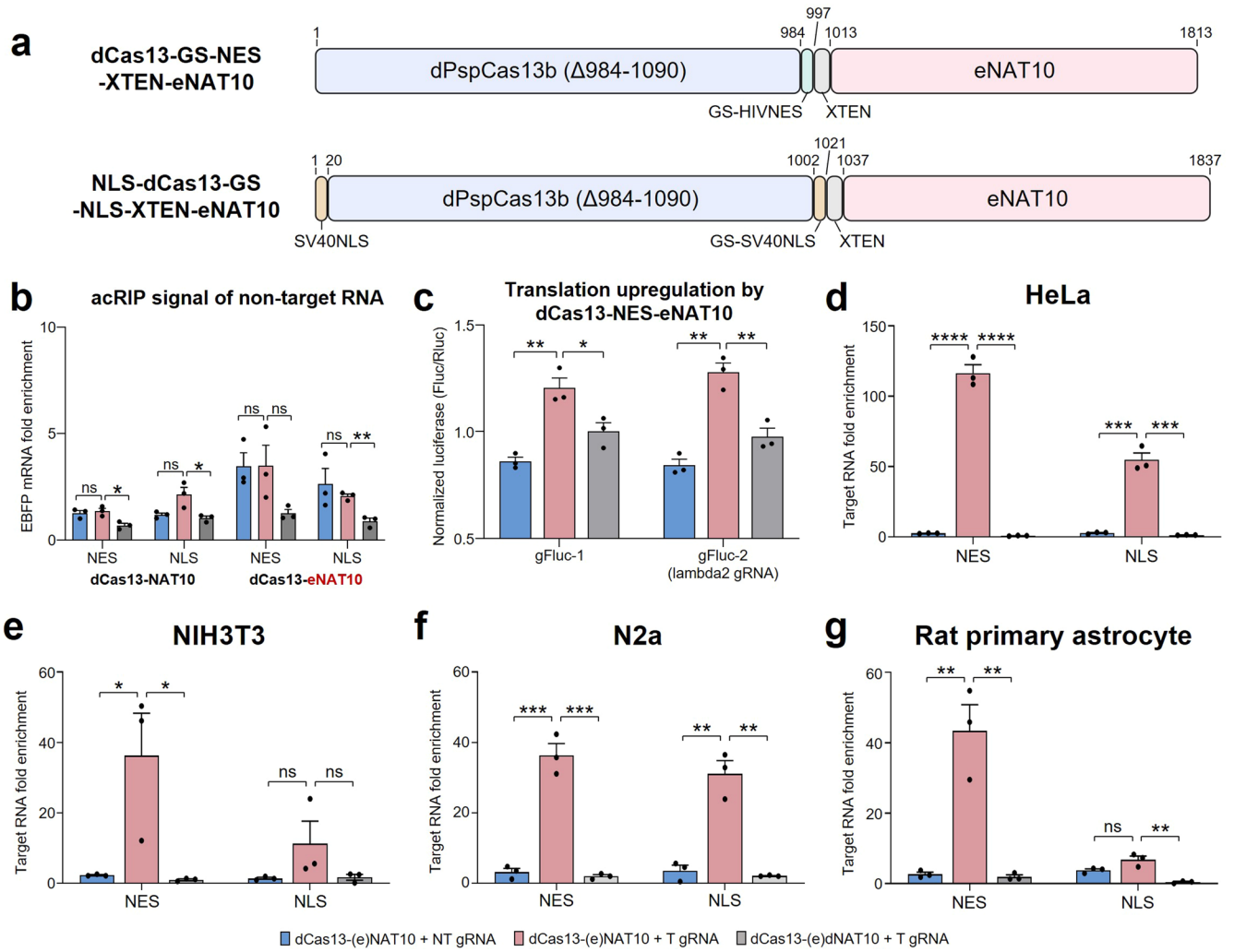

Extended Data Fig. 2 | dPspCas13b-eNAT10 fusion proteins specifically & robustly acetylate target RNA in various cellular contexts. a, Conformation of target RNA acetylation systems used in this study. NES fusion and NLS fusion constructs are represented with amino acid counts. **b**, Non-target EBFP2 reporter RNA acetylation by dCas13-NAT10 and dCas13–eNAT10 fusion proteins in 293 T cells, measured by acRIP-qPCR. EBFP2 mRNA has no binding site for non-targeting gRNA (NT gRNA) nor lambda2-targeting gRNA (T gRNA). Data are presented as the mean ± s.e.m. from three biologically independent replicates. Significance was calculated by two-tailed Student's t-test. ns ($P = 6.20 \times 10^{-1}$, 5.30×10^{-2}, 9.88×10^{-1}, 8.94×10^{-2} and 4.83×10^{-1}, from left to right); *$P < 0.05$ ($P = 1.56 \times 10^{-2}$ and 3.48×10^{-2}, from left to right); **$P < 0.01$ ($P = 3.16 \times 10^{-3}$). **c**, Translation upregulation by luciferase reporter mRNA acetylation in 293 T cells. Firefly luciferase mRNA was targeted by dCas13-NES-eNAT10 with two different gRNAs. Firefly luciferase signals were normalized to control Renilla luciferase signals. Data are presented as the mean ± s.e.m. from three biologically independent replicates. Significance was calculated by two-tailed Student's t-test. *$P < 0.05$ ($P = 3.21 \times 10^{-2}$); **$P < 0.01$ ($P = 2.67 \times 10^{-3}$, $P = 1.13 \times 10^{-3}$ and $P = 6.88 \times 10^{-3}$, from left to right). **d**-**g**, mCherry-lambda2 reporter RNA acetylation by dCas13-eNAT10 fusion proteins in HeLa (**d**), NIH3T3 (**e**), Neuro2a (**f**), and rat primary astrocytes (**g**), measured by acRIP-qPCR. Data are presented as the mean ± s.e.m. from three biologically independent replicates. Significance was calculated by two-tailed Student's t-test. ns ($P = 1.98 \times 10^{-1}$, 2.13×10^{-1} and 5.70×10^{-2}, from panel d to g, from left to right); *$P < 0.05$ ($P = 4.87 \times 10^{-2}$ and 4.38×10^{-2}, from left to right); **$P < 0.01$ ($P = 2.46 \times 10^{-3}$, 1.49×10^{-3}, 5.34×10^{-3}, 5.00×10^{-3} and 3.93×10^{-3}, from panel d to g, from left to right); ***$P < 0.001$ ($P = 4.96 \times 10^{-4}$, 4.42×10^{-4}, 6.32×10^{-4} and 4.73×10^{-4}, from panel d to g, from left to right); ****$P < 0.0001$ ($P = 4.31 \times 10^{-5}$ and 4.06×10^{-5}, from panel **d** to **g**, from left to right).

https://doi.org/10.1038/s41589-025-01922-3

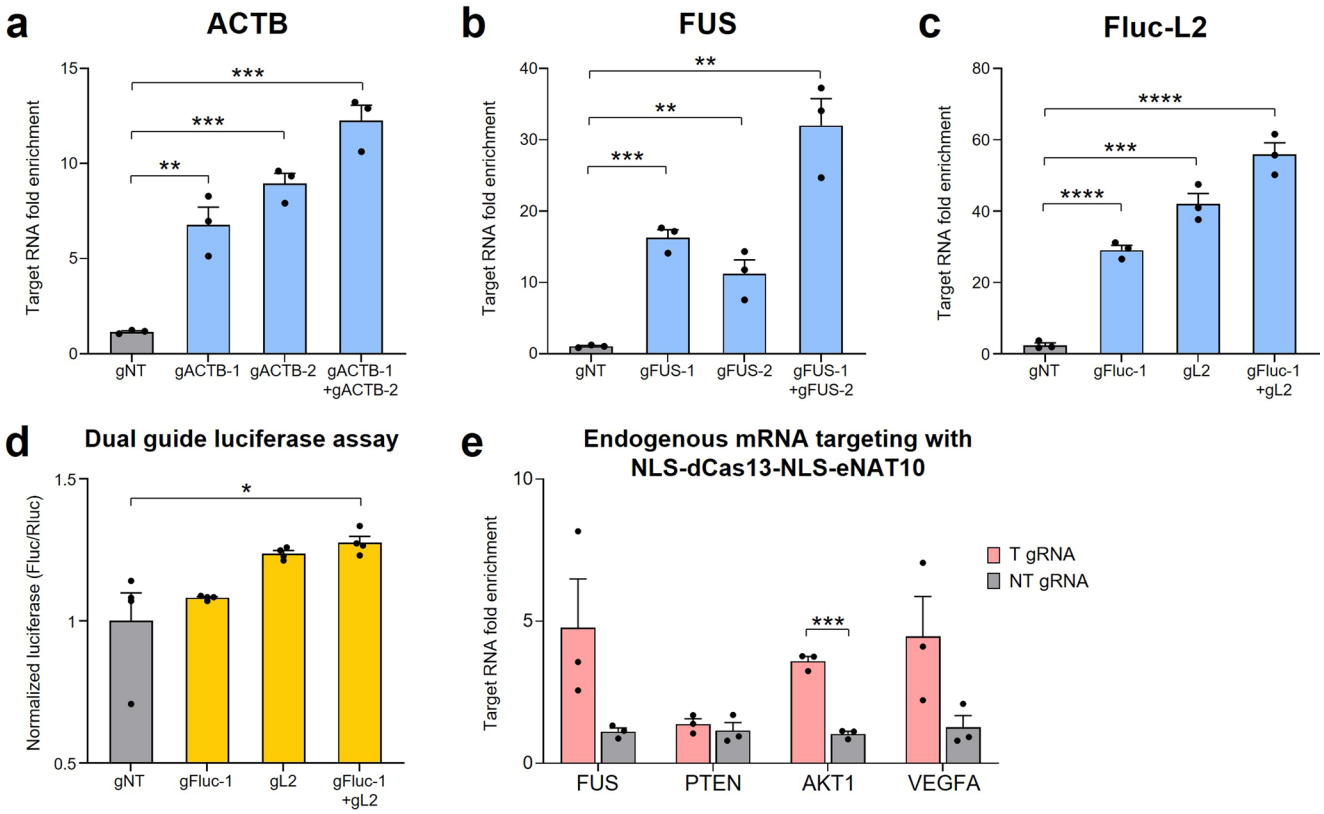

Extended Data Fig. 3 | Targeted RNA acetylation with dual guides and nuclear version of the tool. a–**c**, RNA acetylation level of dCas13-NES-eNAT10 targeted endogenous ACTB (**a**), FUS (**b**), and exogenous Fluc-lambda2 (L2) reporter (**c**), in 293 T cells with annotated gRNAs or dual gRNAs, measured by acRIP-qPCR. Data are presented as the mean ± s.e.m. from three biologically independent replicates. Significance was calculated by two-tailed Student's t-test. **P < 0.01 ($P = 3.51 \times 10^{-3}$, 6.80×10^{-3} and 1.21×10^{-3}, from left to right); ***P < 0.001 ($P = 1.24 \times 10^{-4}$, 1.71×10^{-4}, 1.58×10^{-4} and 1.80×10^{-4}, from left to right); ****P < 0.0001 ($P = 5.53 \times 10^{-5}$ and 8.98×10^{-5}, from left to right). **d**, Translation upregulation of luciferase reporter mRNA upon targeted acetylation in 293 T cells. Fluc-lambda2 reporter was targeted by dCas13-NES-eNAT10 with annotated gRNAs. Firefly luciferase signal was normalized to control Renilla luciferase signal. Data are presented as the mean ± s.e.m. from four biologically independent replicates. Significance was calculated by two-tailed Student's t-test. *P < 0.05 ($P = 3.44 \times 10^{-2}$). **e**, Programmable acetylation of endogenous mRNAs with NLS-dCas13-NLS-eNAT10 in 293 T cells. RNA acetylation signals were measured by acRIP-qPCR. Data are presented as the mean ± s.e.m. from three biologically independent replicates. Significance was calculated by two-tailed Student's t-test. ***P < 0.001 ($P = 1.98 \times 10^{-4}$).

https://doi.org/10.1038/s41589-025-01922-3

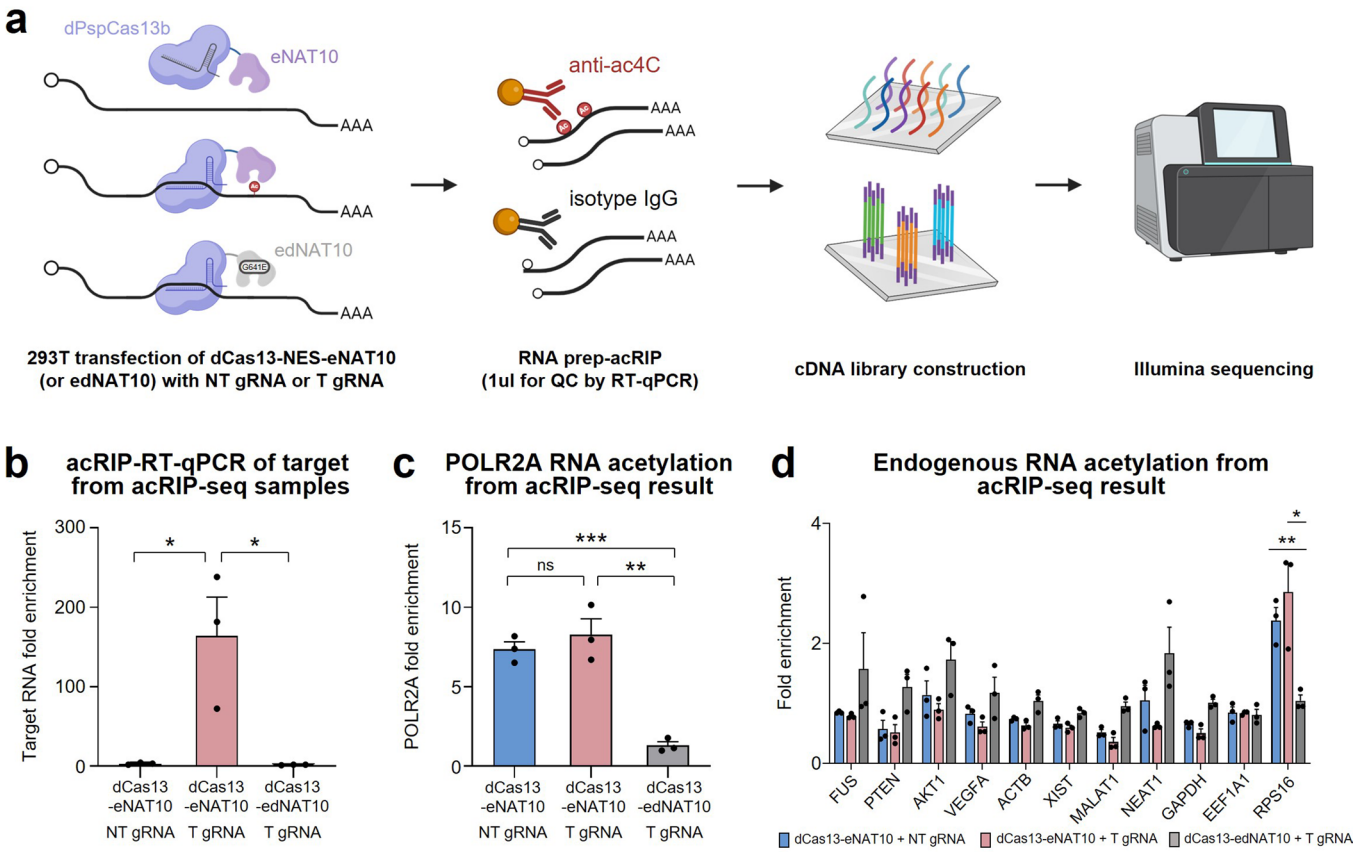

Extended Data Fig. 4 | acRIP-seq analysis of dCas13-NES-eNAT10 transfected 293 T cells. a, Schematic illustration of acRIP-seq for transcriptome-wide off-target analysis. **b**, acRIP-RT-qPCR result of gRNA-targeted mCherry-lambda2 reporter mRNA from acRIP-seq samples. 1ul of acRIP-eluted samples were used as RT-qPCR template, and remaining 19ul was processed to NGS library construction. Data are presented as the mean ± s.e.m. from three biologically independent replicates. Significance was calculated by two-tailed Student's t-test. *P < 0.05 ($P = 2.98 \times 10^{-2}$ and 2.89×10^{-2}, from left to right). **c**, Off-target POLR2A RNA acetylation by dCas13-NES-eNAT10. Fold enrichment values of endogenous POLR2A transcript from acRIP-seq samples are plotted. Data are presented as the mean ± s.e.m. from three biologically independent replicates. Significance was calculated by two-tailed Student's t-test. ns ($P = 4.60 \times 10^{-1}$); **P < 0.01 ($P = 2.58 \times 10^{-3}$); ***P < 0.001 ($P = 3.61 \times 10^{-4}$). **d**, Fold enrichment values of various endogenous transcripts from acRIP-seq samples. Data are presented as the mean ± s.e.m. from three biologically independent replicates. Significance was calculated by two-tailed Student's t-test. *P < 0.05 ($P = 2.00 \times 10^{-2}$); **P < 0.01 ($P = 4.79 \times 10^{-3}$).

https://doi.org/10.1038/s41589-025-01922-3

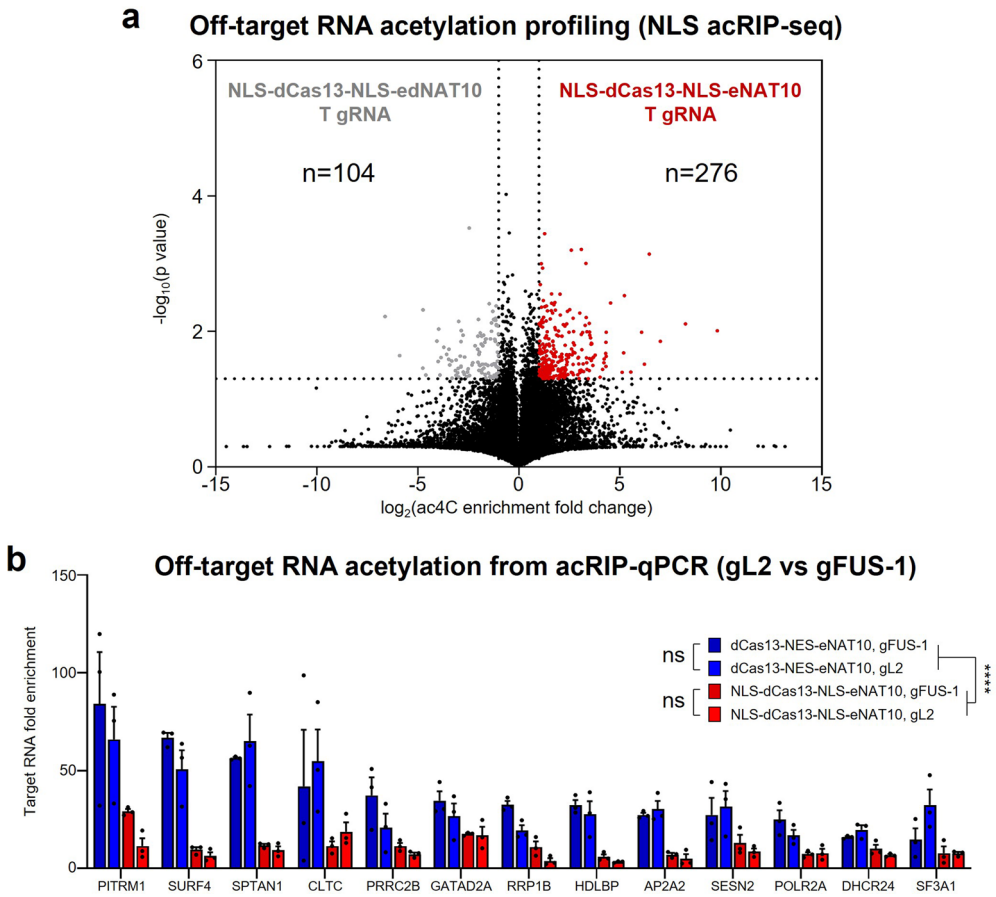

Extended Data Fig. 5 | Off-target RNA acetylation analysis of NES- and NLS- fused dCas13-eNAT10. a, Transcriptome-wide off-target analysis of 293 T transfected with NLS-dCas13-NLS-eNAT10 (or edNAT10), lambda2-targeting gRNA, and mCherry-lambda2 reporter. Numbers of genes with differential ac4C enrichment are annotated at each graph. (acRIP-seq TPM cutoff: 10, p value cutoff: 0.05, ac4C enrichment fold change cutoff: 2-fold) acRIP-seq was performed using two independent biological replicates for each sample group. **b**, Off-target RNA acetylation analysis of highly acetylated and highly expressed genes using acRIP-qPCR. RNA acetylation of specified RNAs were compared using acRIP-qPCR upon transfection of NES or NLS version of the tool, and upon exogenous mCherry-lambda2 reporter targeting or endogenous FUS targeting context. Data are presented as the mean ± s.e.m. from three biologically independent replicates. Significance was calculated by two-tailed paired Student's t-test. ns ($P = 4.35 \times 10^{-1}$ and 7.07×10^{-2}, from top to bottom); ****$P < 0.0001$.

https://doi.org/10.1038/s41589-025-01922-3

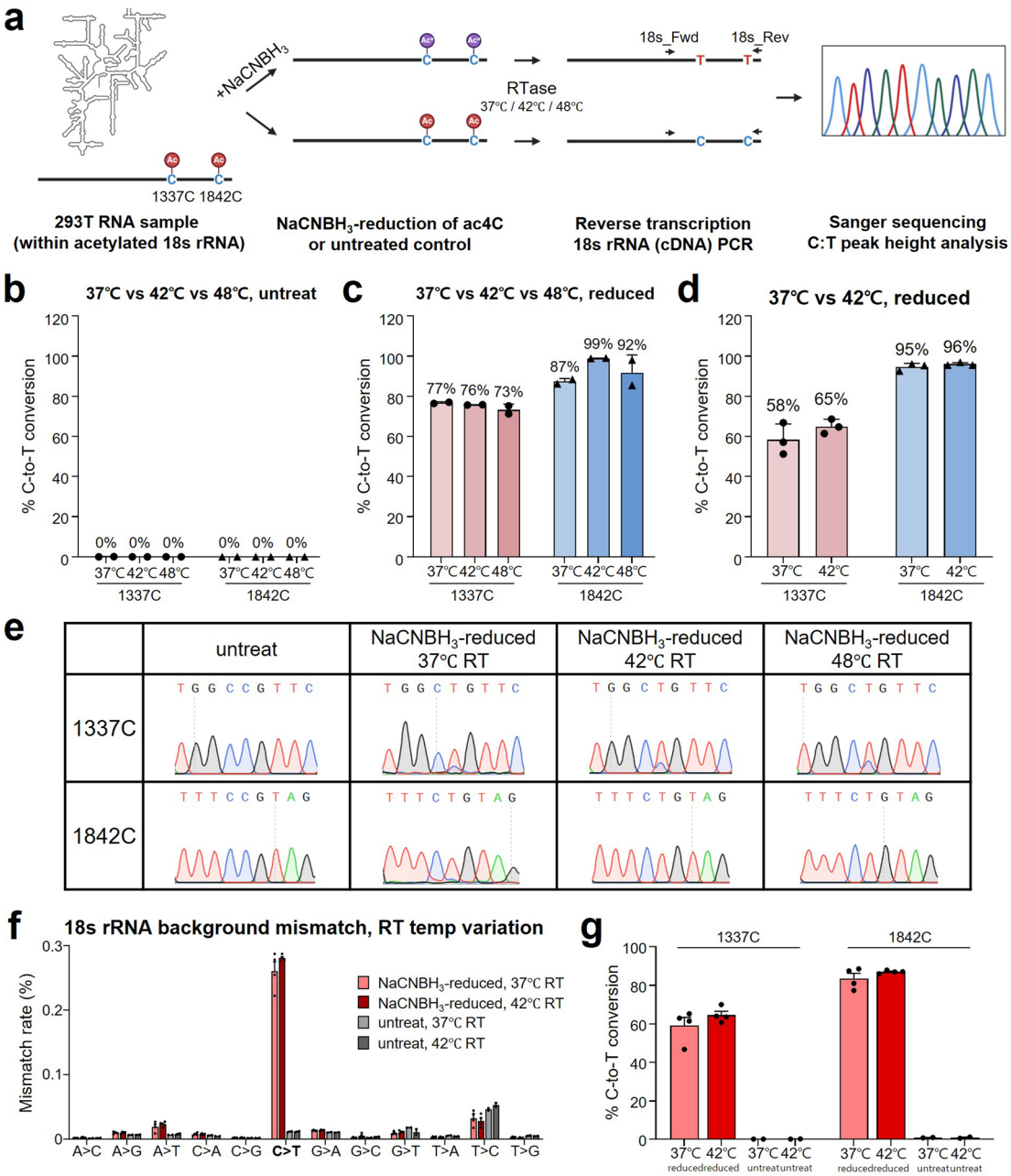

Extended Data Fig. 6 | Optimization of acRIP-NaCNBH3-RT-PCR-sequencing for single-base ac4C mapping. a, Schematic illustration of reverse transcription temperature optimization for NaCNBH3-treated RNA samples. Two conserved ac4C residues of human 18 s rRNA (1337 C, 1842C) were analyzed with Sanger sequencing. **b**–**d**, C-to-T conversion level of 18 s rRNA 1337 C and 1842C with (**c**,**d**) or without (**b**) NaCNBH3 treatment. Reverse transcription temperatures for each sample group are annotated below. C-to-T conversion level is annotated above each bar. Data are presented as the mean ± s.e.m. from two biologically independent replicates. **e**, Representative Sanger chromatogram of 18 s rRNA 1337 C and 1842C upon NaCNBH3 treatment and reverse transcription in different temperatures. **f**, Mismatch rate of all types of conversions in amplicon sequencing analysis of 18 s rRNA upon different RT temperatures. Data are presented as the mean ± s.e.m. from four (NaCNBH3-reduced) or two (untreat) biologically independent replicates. **g**, C-to-T conversion rate of 18 s rRNA 1337 C and 1842C in amplicon sequencing results from f. Data are presented as the mean ± s.e.m. from four (NaCNBH3-reduced) or two (untreat) biologically independent replicates.

https://doi.org/10.1038/s41589-025-01922-3

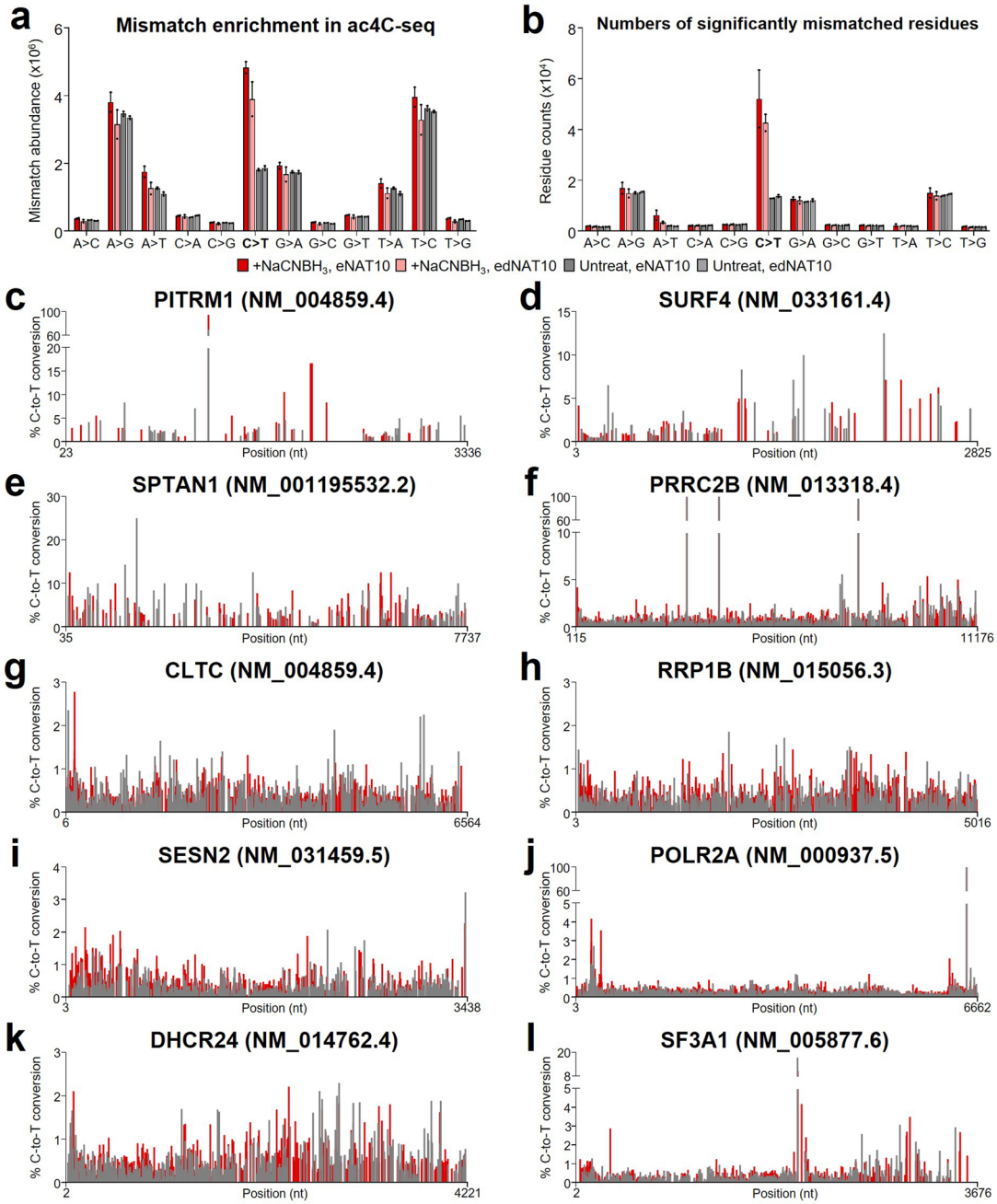

Extended Data Fig. 7 | Off-target RNA acetylation profiling by transcriptome-wide ac4C-seq. a, b, Background mismatch analysis of ac4C-seq. Total RNA of 293 T cells transfected with dCas13-NES-e(d)NAT10 was treated with NaCNBH3, reverse-transcribed, and sequenced. Total number of mismatches (**a**), and numbers of significantly mismatched residues (**b**) compared to reference human transcriptome. Significantly mismatched residues are defined as, read numbers > 10, mismatched read numbers > 3, and mismatch rate > 0.0125. Data are presented as the mean ± s.e.m. from two biologically independent replicates. **c–l**, Average ac4C-seq C-to-T conversion rate of off-target transcripts. C-to-T mismatch rate of annotated genes from dCas13-NES-eNAT10 transfected sample (red) and dCas13-NES-edNAT10 transfected sample (gray) are shown. Data are presented as the mean from two biologically independent replicates.

https://doi.org/10.1038/s41589-025-01922-3

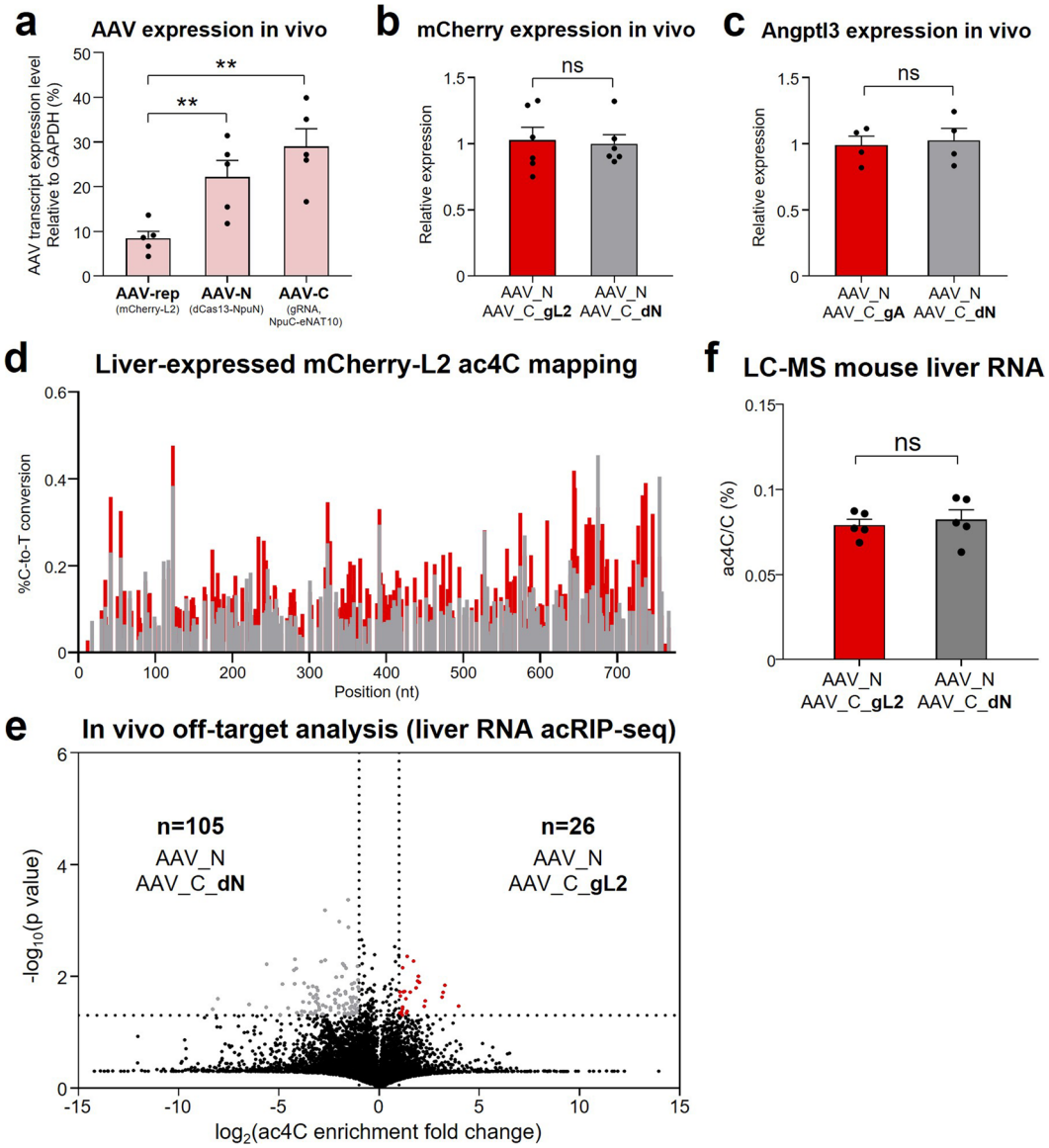

Extended Data Fig. 8 | In vivo RNA acetylation with AAV-encoded dCas13-eNAT10. a, Expression of AAV transgenes in vivo. Reporter AAV (AAV_rep), dCas13-NpuN (AAV_N) and NpuC-eNAT10 (AAV_C) transcript expression was measured with qPCR from mouse liver bulk RNA samples. Data are presented as the mean ± s.e.m. from five biologically independent replicates. Significance was calculated by two-tailed Student's t-test. **P < 0.01 ($P = 9.02 \times 10^{-3}$ and 1.40×10^{-3}, from left to right). **b**, Relative protein expression level of mCherry targeted with tool AAV in mouse liver, measured by Western blot. Expression was normalized by constitutively expressed beta actin protein. Data are presented as the mean ± s.e.m. from six biologically independent replicates. Significance was calculated by two-tailed Student's t-test. ns ($P = 9.79 \times 10^{-1}$). **c**, Relative protein expression level of Angptl3 targeted with tool AAV in mouse liver, measured by Angptl3 ELISA of serum samples. Data are presented as the mean ± s.e.m. from four biologically independent replicates. Significance was calculated by two-tailed Student's t-test. ns ($P = 7.64 \times 10^{-1}$). **d**, Single base resolution ac4C mapping using NaCNBH3-RT-PCR-sequencing. C-to-T conversion levels of mCherry-L2 reporter transduced with tool AAVs in mouse liver. Red, catalytically active AAV_C transduced samples, gray, catalytically inactive AAV_C transduced samples. Data are presented as the mean rom three biologically independent replicates. **e**, Transcriptome-wide off-target analysis mouse liver transduced with tool AAV using acRIP-seq. Numbers of genes with differential ac4C enrichment are annotated at each graph. (acRIP-seq TPM cutoff: 10, p value cutoff: 0.05, ac4C enrichment fold change cutoff: 2-fold) acRIP-seq was performed using two independent biological replicates for each sample groups. **f**, Quantification of ac4C/C ratio in total RNA from tool AAV-transduced mouse liver by LC-QQQ-MS. Data are presented as the mean ± s.e.m. from five biologically independent replicates. Significance was calculated by two-tailed Student's t-test. ns ($P = 6.57 \times 10^{-1}$).

https://doi.org/10.1038/s41589-025-01922-3

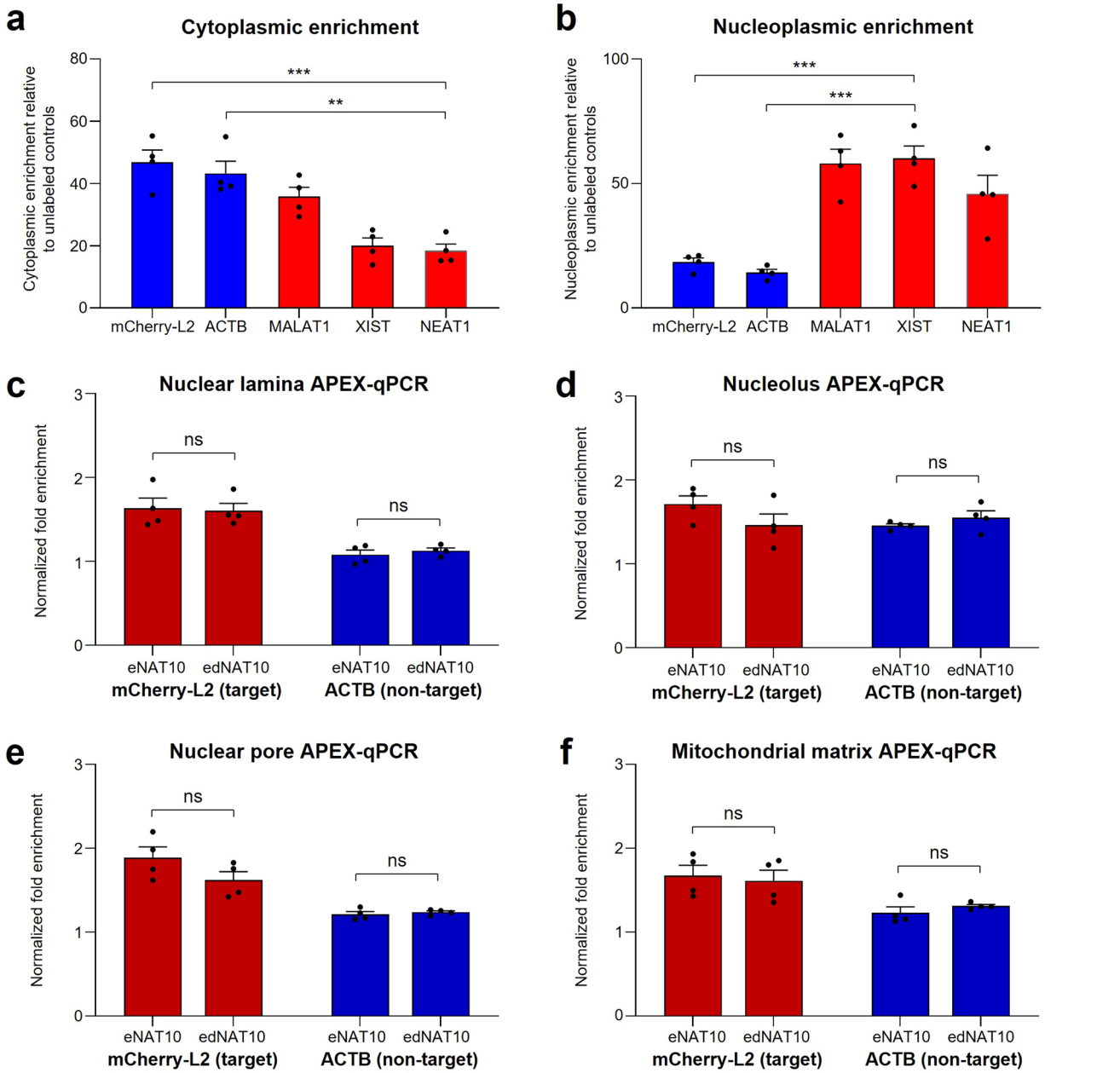

Extended Data Fig. 9 | Subcellular RNA labeling with APEX2. a, b, Subcellular enrichment of mCherry-lambda2 reporter, endogenous ACTB, MALAT1, XIST, and NEAT1 in cytoplasm (**a**) and nucleus (**b**). Data are presented as the mean ± s.e.m. from four biologically independent replicates. Significance was calculated by two-tailed Student's t-test. **P < 0.01 ($P = 1.51 \times 10^{-3}$); ***P < 0.001 ($P = 7.26 \times 10^{-4}$, 2.27×10^{-4} and 1.18×10^{-4}, from left to right). **c**–**f**, Subcellular enrichment of mCherry-lambda2 (target) and ACTB (non-target) transcripts in nuclear lamina (**c**), nucleolus (**d**), nuclear pore (**e**), and mitochondrial matrix (**f**), measured by streptavidin pulldown of APEX2-labeled RNA and RT-qPCR. Raw enrichment value was normalized by GAPDH enrichment value. Data are presented as the mean ± s.e.m. from four biologically independent replicates. Significance was calculated by two-tailed Student's t-test. ns ($P = 8.44 \times 10^{-1}$, 4.73×10^{-1}, 1.73×10^{-1}, 2.86×10^{-1}, 1.52×10^{-1}, 5.14×10^{-1}, 7.41×10^{-1} and 4.14×10^{-1}, from panel **c** to **f**, from left to right).

https://doi.org/10.1038/s41589-025-01922-3

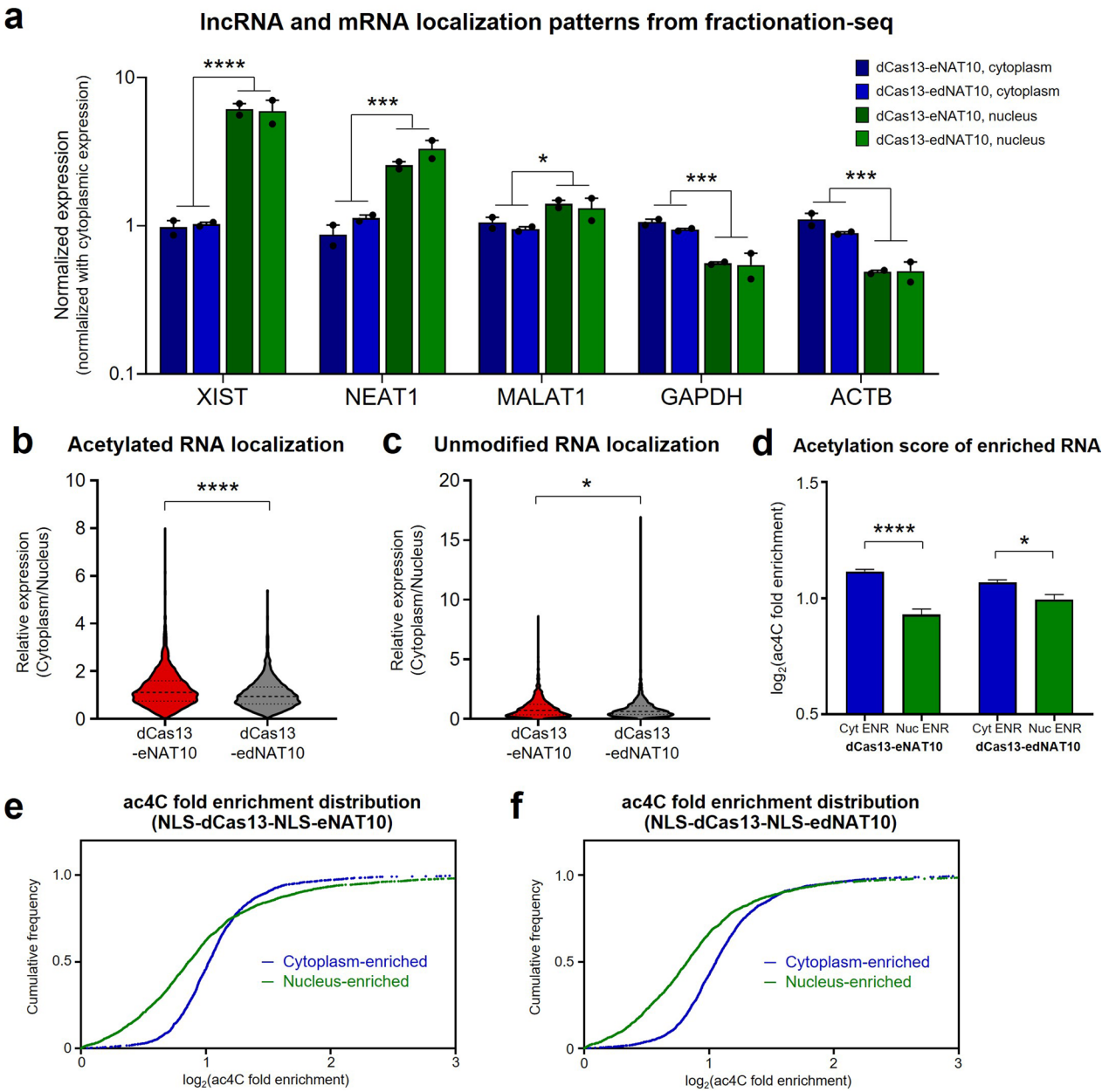

Extended Data Fig. 10 | Nucleus-cytoplasm fractionation and sequencing profiles subcellular transcriptome. a, Expression level of selected lncRNA and mRNA in fractionation-seq. Expression level was individually normalized by the average cytoplasmic expression level of each transcript. Data are presented as the mean ± s.e.m. from two biologically independent replicates. Significance was calculated by two-tailed Student's t-test. *P < 0.05 (P = 1.96×10^{-2}); ***P < 0.001 (P = 7.51×10^{-4}, 2.77×10^{-4} and 8.21×10^{-4}, from left to right); ****P < 0.0001 (P = 5.53×10^{-5}). **b, c**, Relative localization of acetylated (**b**) and unmodified (**c**) RNA in fractionation-seq. Genes with average fold enrichment > 2 from NLS acRIP-seq (in Extended Data Fig. 5a, n = 1,785, **b**) average fold enrichment < 0.5 from NLS acRIP-seq (n = 1,503,**c**) were plotted. Medians are indicated by thick dotted lines and quartile ranges (25th and 75th percentiles) are indicated by thinner dotted lines. Significance was calculated by Mann-Whitney U test. *P < 0.05 (P = 2.23×10^{-2}); ****P < 0.0001. **d**, Acetylation level of transcripts enriched in cytoplasm and nucleus from NLS-dCas13-NLS-e(d)NAT10 transfected cells. Cytoplasm-enriched upon dCas13-eNAT10 (n = 2,316), nucleus-enriched upon dCas13-eNAT10 (n = 2,001), Cytoplasm-enriched upon dCas13-edNAT10 (n = 1,634), and nucleus-enriched upon dCas13-edNAT10 (n = 2,254). Data are presented as the mean ± s.e.m. and significance was calculated by one-way ANOVA. *P < 0.05 (P = 1.62×10^{-2}); ****P < 0.0001. **e, f**, Cumulative distribution plot showing differential ac4C fold enrichment of transcripts with cytoplasm and nuclear enrichment in NLS-dCas13-NLS-eNAT10 (**e**) and NLS-dCas13-NLS-edNAT10 (**f**) transfected 293 T cells.

nature portfolio

Corresponding author(s): Won Do Heo

Last updated by author(s): Apr 9, 2025

Reporting Summary

Nature Portfolio wishes to improve the reproducibility of the work that we publish. This form provides structure for consistency and transparency in reporting. For further information on Nature Portfolio policies, see our Editorial Policies and the Editorial Policy Checklist.

Statistics

For all statistical analyses, confirm that the following items are present in the figure legend, table legend, main text, or Methods section.

n/a	Confirmed
☐	☒ The exact sample size (*n*) for each experimental group/condition, given as a discrete number and unit of measurement
☐	☒ A statement on whether measurements were taken from distinct samples or whether the same sample was measured repeatedly
☐	☒ The statistical test(s) used AND whether they are one- or two-sided *Only common tests should be described solely by name; describe more complex techniques in the Methods section.*
☒	☐ A description of all covariates tested
☐	☒ A description of any assumptions or corrections, such as tests of normality and adjustment for multiple comparisons
☐	☒ A full description of the statistical parameters including central tendency (e.g. means) or other basic estimates (e.g. regression coefficient) AND variation (e.g. standard deviation) or associated estimates of uncertainty (e.g. confidence intervals)
☐	☒ For null hypothesis testing, the test statistic (e.g. *F*, *t*, *r*) with confidence intervals, effect sizes, degrees of freedom and *P* value noted *Give P values as exact values whenever suitable.*
☒	☐ For Bayesian analysis, information on the choice of priors and Markov chain Monte Carlo settings
☒	☐ For hierarchical and complex designs, identification of the appropriate level for tests and full reporting of outcomes
☐	☒ Estimates of effect sizes (e.g. Cohen's *d*, Pearson's *r*), indicating how they were calculated

Our web collection on statistics for biologists contains articles on many of the points above.

Software and code

Policy information about availability of computer code

Data collection	Nikon A1R confocal microscope mounted on a Nikon Eclipse Ti body with a Nikon CFI plan Apochromat VC 60X/1.4 numerical aperture and NIS-elements AR 64-bit version 3.21 were used for fluorescence imaging. Tecan spark 10M microplate reader is used for luciferase assay. Bio-rad CFXMaestro 96 instrument was used for qPCR. BD LSRFortessa and BD FACSDiva software were used for flow cytometry. Odyssey CLx imaing system and Image Studio v5.2 were used for Western blot. RNA sequencing was conducted with Illumina NovaSeq system.
Data analysis	Protein structure was predicted using AlphaFold2 and analyzed with PyMOL2.5.2. Imaging data was analyzed in Nikon imaging software 5.21. Western blot bands were quantified densitometrically using ImageJ version 1.54g. Flow cytometry results were analyzed with FlowJo v10. Prior to RNA seqeuncing data analysis, adapter sequences were removed and poor-quality bases were trimmed using Trimmomatic v0.38 and v0.40. Cleaned reads were aligned to the Homo sapiens genome (GRCh38) using HISAT v2.1.0, based on HISAT and Bowtie2 implementations. Aligned data were sorted and indexed using SAMtools v1.9. After alignment, the transcripts were assembled and quantified using StringTie v2.1.3b. Browser shots of sequenced reads were obtained from IGV v.2.17.4 software. Data was analyzed in Graphpad Prism 9 and Microsoft Excel for Microsoft 365 (version 2503).

For manuscripts utilizing custom algorithms or software that are central to the research but not yet described in published literature, software must be made available to editors and reviewers. We strongly encourage code deposition in a community repository (e.g. GitHub). See the Nature Portfolio guidelines for submitting code & software for further information.

Data

Policy information about availability of data

All manuscripts must include a data availability statement. This statement should provide the following information, where applicable:

- Accession codes, unique identifiers, or web links for publicly available datasets
- A description of any restrictions on data availability
- For clinical datasets or third party data, please ensure that the statement adheres to our policy

The RNA-seq, acRIP-seq, ac4C-seq, and fractionation-seq data generated in this study are deposited in the NCBI Gene Expression Omnibus (GEO) under accession number GSE293920. The hg38 (GRCh38.p14) and mm39 (GRCm39) reference genomes were used for RNA-seq alignment in HEK293T cells and mouse tissues.

Human research participants

Policy information about studies involving human research participants and Sex and Gender in Research.

Reporting on sex and gender	N/A
Population characteristics	N/A
Recruitment	N/A
Ethics oversight	N/A

Note that full information on the approval of the study protocol must also be provided in the manuscript.

Field-specific reporting

Please select the one below that is the best fit for your research. If you are not sure, read the appropriate sections before making your selection.

☒ Life sciences ☐ Behavioural & social sciences ☐ Ecological, evolutionary & environmental sciences

For a reference copy of the document with all sections, see nature.com/documents/nr-reporting-summary-flat.pdf

Life sciences study design

All studies must disclose on these points even when the disclosure is negative.

Sample size	For in vitro experiments, two to four biological replicates were used for statistical analysis, except for the representative Sanger sequencing data from Supplementary Figure 8. For in vivo experiments, four to six biological replicates were used for statistical analysis. These sample sizes were chosen based on similar studies in the field.
Data exclusions	No data was excluded.
Replication	Number of replicates are noted at figures by individual dots, and/or specified at figure legends.
Randomization	Cells and animals are randomly assigned to experimental groups.
Blinding	Blinding is irrelevant to the study since all replicates were prepared uniformly by researchers who also analyzed the results.

Reporting for specific materials, systems and methods

We require information from authors about some types of materials, experimental systems and methods used in many studies. Here, indicate whether each material, system or method listed is relevant to your study. If you are not sure if a list item applies to your research, read the appropriate section before selecting a response.

Materials & experimental systems

n/a	Involved in the study
☐	☒ Antibodies
☐	☒ Eukaryotic cell lines
☒	☐ Palaeontology and archaeology
☐	☒ Animals and other organisms
☒	☐ Clinical data
☒	☐ Dual use research of concern

Methods

n/a	Involved in the study
☒	☐ ChIP-seq
☐	☒ Flow cytometry
☒	☐ MRI-based neuroimaging

Antibodies

Antibodies used

Rabbit anti-ac4C (Abcam, ab252215), rabbit isotype IgG (CST, #3900) were used for acRIP. Rabbit anti-DYKDDDDK Tag (1:1000; CST, #14793), mouse anti-FUS (1:1000; Abcam, ab283272), rabbit anti-PTEN (1:5000; Abcam, ab32199), rat anti-mCherry (1:1000; Invitrogen, M11217), mouse anti-GAPDH (1:5000; Invitrogen, MA5-15738), and rabbit anti-β-Actin (1:1000; CST, #4970), IRDye 680RD-conjugated donkey anti-rabbit (1:10000; LI-COR, 926-68073), IRDye 800CW-conjugated donkey anti-rabbit (1:10000; LI-COR, 926-32213), IRDye 680RD-conjugated donkey anti-mouse (1:10000; LI-COR, 926-68072), IRDye 800CW-conjugated goat anti-rat (1:10000; LI-COR, 926-32219), and IRDye 800CW-conjugated donkey anti-mouse (1:10000; LI-COR, 926-32212) were used for Western blot. Rabbit anti-DYKDDDDK Tag (CST, #14793), rat anti-DYKDDDDK Tag (BioLegend, 637301), rabbit anti-acetyl lysine (Abcam, ab80178), Alexa Fluor 488-conjugated goat anti-rabbit (Thermo Fisher, A11034), Alexa Fluor 594-conjugated goat anti-rabbit (Thermo Fisher, A11037), and Alexa Fluor 488-conjugated goat anti-rat (Thermo Fisher, A11006) were used for ICC.

Validation

Antibodies were only chosen if there were validated references available. Rabbit anti-ac4C & rabbit isotype IgG (PMID: 30449621), rabbit anti-DYKDDDDK Tag (PMID: 38253589), rabbit anti-PTEN (PMID: 32341353), rat anti-mCherry (PMID: 37217469), mouse anti-GAPDH (PMID: 37730840), rabbit anti-β-Actin (PMID: 30596540), rat anti-DYKDDDDK Tag (PMID: 30392931), and rabbit anti-acetyl lysine (PMID: 35875610). For mouse anti-FUS, we have selected the KO-validated antibody from the manufacturer's website.

Eukaryotic cell lines

Policy information about cell lines and Sex and Gender in Research

Cell line source(s)

HEK293T (CRL-11268), HeLa (CCL-2), NIH/3T3 (CRL-1658) and Neuro-2a (CCL-131) cell lines were acquired from ATCC. Rat primary astrocytes were obtained from embryonic day 18 (E18) embryos were obtained from a pregnant Sprague Dawley rat (Orient Bio).

Authentication

None of the cell lines used were authenticated.

Mycoplasma contamination

The cell line tested negative for mycoplasma contamination.

Commonly misidentified lines
(See ICLAC register)

No commonly misidentified cell lines were used.

Animals and other research organisms

Policy information about studies involving animals; ARRIVE guidelines recommended for reporting animal research, and Sex and Gender in Research

Laboratory animals

4- to 5-week old male B6SJL mice were purchased from Raonbio. All mice were housed under a 12:12 light-dark cycle at room temperature and 40% humidity.

Wild animals

No wild animals were used in the study.

Reporting on sex

Only male mice were used for experiments.

Field-collected samples

No field-collected samples were used in the study.

Ethics oversight

Animal experiments and treatments followed the guidelines of the Institutional Animal Care and Use Committees (IACUC) at Korea Advanced Institute of Science and Technology (KAIST). The approval number for this study is KA2024-007-v3.

Note that full information on the approval of the study protocol must also be provided in the manuscript.

Flow Cytometry

Plots

Confirm that:

☒ The axis labels state the marker and fluorochrome used (e.g. CD4-FITC).

☒ The axis scales are clearly visible. Include numbers along axes only for bottom left plot of group (a 'group' is an analysis of identical markers).

☒ All plots are contour plots with outliers or pseudocolor plots.

☒ A numerical value for number of cells or percentage (with statistics) is provided.

Methodology

Sample preparation	Transfected HEK293T cells in a 24-well plates were detached with trypsin and resuspended in ice-cold FACS buffer.
Instrument	BD LSRFortessa flow cytometer.
Software	BD FACSDiva software and FlowJo v10.
Cell population abundance	Singlet cells were gated by FSC-H and FSC-A, and live cells were gated using FSC-A and SSC-A.
Gating strategy	Singlet cells were gated by FSC-H and FSC-A, followed by live cell gating using FSC-A and SSC-A. Live and single cells were analyzed with SSC-A vs PE-Texas Red-A (for mCherry fluorescence) and SSC-A vs Pacific Blue-A (for EBFP2 fluorescence).

☒ Tick this box to confirm that a figure exemplifying the gating strategy is provided in the Supplementary Information.